



1 Do Loop Current Eddies stimulate productivity in the Gulf of Mexico?

2 Pierre Damien^(1,2), Julio Sheinbaum⁽¹⁾, Orens Pasqueron de Fommervault⁽¹⁾, Julien Jouanno⁽³⁾, Lorena

3 Linacre⁽⁴⁾, Olaf Duteil⁽⁵⁾

4 ⁽¹⁾ Departamento de Oceanografía Física, Centro de Investigación Científica y de Educación Superior
5 de, Ensenada, México,

6 ⁽²⁾ University of California, Los Angeles, CA

7 ⁽³⁾ LEGOS, Université de Toulouse, IRD, CNRS, CNES, UPS, Toulouse, France,

8 ⁽⁴⁾ Departamento de Oceanografía Biológica, Centro de Investigación Científica y de Educación
9 Superior de Ensenada, México,

10 ⁽⁵⁾ GEOMAR Helmholtz Centre for Ocean Research, Kiel, Germany.

11 Corresponding author: Pierre Damien (pdamien@ucla.edu)

12 **Key Points :**

- 13 • LCEs trigger a local phytoplankton biomass increase in winter.
- 14 • Chlorophyll variability at surface does not reflect the seasonal cycle of the depth-integrated
15 biomass.
- 16 • Convective mixing and Ekman pumping are key mechanisms to preferentially supply nutrient
17 toward the euphotic layer in LCEs.



18 **Abstract**

19 Surface chlorophyll concentrations inferred from satellite images suggest a strong influence of
20 the mesoscale activity on biogeochemical variability within the oligotrophic regions of the Gulf of
21 Mexico (GoM). More specifically, long-living anticyclonic Loop Current Eddies (LCEs) are shed
22 episodically from the Yucatan Channel and propagate westward. This study addresses the
23 biogeochemical response of the LCEs to seasonal forcing and show their role in driving phytoplankton
24 biomass distribution in the GoM. Using an eddy resolving ($1/12^\circ$) interannual regional simulation
25 based on the coupled physical-biogeochemical model NEMO-PISCES that yields a realistic
26 representation of the surface chlorophyll distribution, it is shown that the LCEs foster a large biomass
27 increase in winter in the upper ocean. The primary production in the LCEs is larger than the average
28 rate in the surrounding open waters of the GoM. This behavior cannot be directly identified from
29 surface chlorophyll distribution alone since LCEs are associated with a negative surface chlorophyll
30 anomaly all year long. This anomalous biomass increase in the LCEs is explained by the mixed-layer
31 response to winter convective mixing that reaches deeper and nutrient-rich waters.



32 **I/ Introduction**

33 Historical satellite ocean color observations of the deep waters of the Gulf of Mexico (roughly
34 delimited by the 200m isobath and from hereafter referred to as GoM open-waters) indicate low surface
35 chlorophyll concentrations ([CHL]), low biomass and low primary productivity (Müller-Karger et al.,
36 1991; Biggs and Ressler, 2001; Salmerón-García et al., 2011). The GoM open-waters are mostly
37 oligotrophic, as confirmed by more recent bio-optical in-situ measurements from autonomous floats
38 (Green et al., 2014; Pasqueron de Fommervault et al., 2017; Damien et al., 2018). The surface
39 chlorophyll concentration in the GoM open-waters exhibits a clear seasonal cycle which is primarily
40 triggered by the seasonal variation of the mixed layer depth (Müller-Karger et al., 2015) and river
41 discharges (Brokaw et al., 2019). In tandem, the seasonal cycle is strongly modulated by the energetic
42 mesoscale dynamic activity which shapes the distribution of biogeochemical properties (Biggs and
43 Ressler, 2001; Pasqueron de Fommervault et al., 2017). This mesoscale activity is dominated by the
44 large and long-living Loop Currents Eddies (LCEs) which are shed episodically by the Loop Current
45 (Weisberg and Liu, 2017) and constitute the most energetic circulation features in the GoM
46 (Sheinbaum et al., 2016; Sturges & Leben, 2000).

47 Mesoscale activity (see McGillicuddy et al., 2016 for a review) modulates the phytoplankton
48 biomass distribution (Siegel et al., 1999; Doney et al., 2003; Gaube et al., 2014; Mahadevan, 2014) and
49 the ecosystem functioning (McGillicuddy et al., 1998, Oschlies and Garcon, 1998, Garcon et al., 2001).
50 Specifically, the ability of the mesoscale eddies to enhance vertical fluxes of nutrients is determinant in
51 sustaining the observed phytoplankton growth rate in oligotrophic regions such as the GoM open-
52 waters, where the phytoplankton primary production is limited by nutrient availability in the euphotic
53 layer (McGillicuddy and Robinson 1997; McGillicuddy et al., 1998; Oschlies and Garcon, 1998).



54 The upward doming of isopycnals in cyclonic eddies and downward depressions in anticyclonic
55 eddies, also known as “eddy-pumping”, occur when the eddies are strengthening (Siegel et al., 1999,
56 Klein and Lapeyre, 2009) and produce a nutrient vertical transport. This has been historically proposed
57 as the dominant mechanism controlling the mesoscale biogeochemical variability, as it induces a
58 reduction of productivity in the anticyclone and an increase in cyclones. This paradigm is however
59 challenged by observations of enhanced surface chlorophyll concentrations in anticyclonic eddies
60 (Gaube et al., 2014), particularly during winter (Dufois et al., 2016). As a plausible explanation, eddy-
61 wind interactions may significantly modulate vertical fluxes through Ekman transport divergence
62 within the eddies (Martin and Richards, 2001, Gaube et al., 2013, 2015). This mechanism is
63 responsible for a downwelling in the core of cyclones and an upwelling in the core of anticyclones.
64 Dufois et al. (2014, 2016) link these observations to a deeper mixed layer in anticyclonic eddies. This is
65 explained by the eddy-driven modulation of the upper ocean stratification which directly affects the
66 winter convective mixing (He et al., 2017). Observed mixed layers tend to be deeper in anticyclones
67 than in cyclones (Williams, 1998; Kouketsu et al., 2012) and vertical nutrient fluxes to the euphotic
68 layer are potentially enhanced in anticyclones during periods prone to convection (e.g. winter in the
69 GoM). Although some consensus exists on the fundamental role of anticyclonic eddies on the
70 productivity of oligotrophic ocean regions, large uncertainties remain regarding the relative importance
71 of the different mechanisms involved in the biogeochemical responses.

72 Besides, in-situ measurements in oligotrophic regions have shown that the surface [CHL]
73 variability, observed from ocean color satellite imagery, is not necessarily representative of the total
74 phytoplankton (carbon) biomass variability in the water column (Siegel et al., 2013; Mignot et al.,
75 2014). In particular, a surface [CHL] winter increase, may result from physiological mechanisms (i.e.
76 modification of the ratio of [CHL] to phytoplankton carbon biomass) or from a vertical redistribution



77 of the phytoplankton (Mayot et al., 2017) rather than from changes in the biomass content. It is not
78 clear yet which of these hypotheses holds in oligotrophic regions, and more specifically in the GoM
79 open-waters where this issue has been addressed by in-situ sub-surface [CHL] observations (Pasqueron
80 de Fommervault et al., 2017). Most of the studies focusing on chlorophyll variability use surface (or
81 near-surface) [CHL] as a proxy for phytoplankton biomass and interpret a [CHL] increase as an
82 effective biomass production. Only a few studies considered the vertically integrated responses (Dufois
83 et al., 2017; Guo et al., 2017; Huang and Xu, 2018) emphasizing the importance of considering the
84 eddy impact on the subsurface.

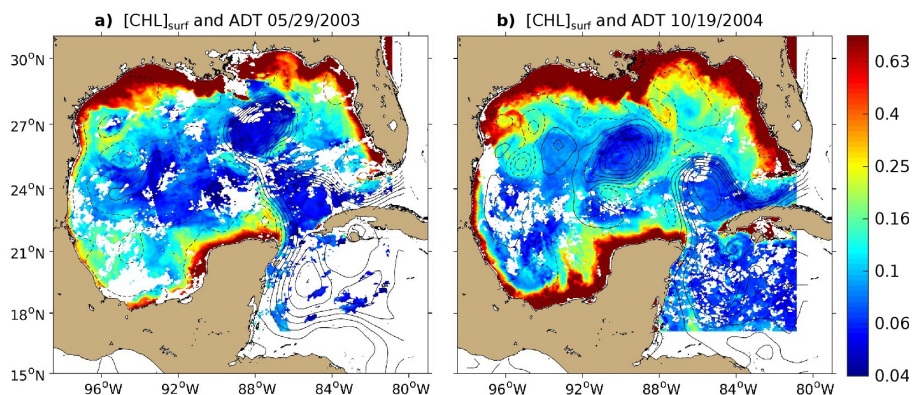
85 The objective of this study is to better understand the role of LCEs in driving [CHL] distribution
86 and variability within the GoM open-waters. Material and methods used in this study are presented in
87 section 2. In section 3, the imprint of the LCEs on the surface [CHL] distribution is inferred from
88 satellite ocean color observations. Since these measurements are confined to the oceanic surface layer
89 and do not allow access to the vertical properties of LCEs, we complete the analysis with a coupled
90 physical-biogeochemical simulation (subsections 2 and 3). Particular attention is paid to the validation
91 of the modeled LCE dynamical structures and surface [CHL] anomalies. In the last section, we propose
92 to disentangle the mesoscale mechanisms controlling the seasonal cycle of the [CHL] vertical profile in
93 LCEs. The model also enables to assess both abiotic and biotic processes and physical-biogeochemical
94 interactions that can be difficult to address with in-situ observations only.

95 **II/ Material and methods**

96 **II.1/ The coupled physical-biogeochemical model**



97 The simulation analyzed in this study (referred as GOLFO12-PISCES) has been described and
98 compared with observations in Damien et al. (2018). It relies on a physical-biogeochemical coupled
99 model based on the ocean model NEMO (Nucleus for European Modeling of the Ocean, version 3.6;
100 Madec, 2016) and the biogeochemical model PISCES (Pelagic Interaction Scheme for Carbon and
101 Ecosystem Studies; Aumont and Bopp, 2006; Aumont et al., 2015). The model grid covers the GoM
102 and the western part of the Cayman Sea (Fig 1) with a $1/12^\circ$ horizontal resolution (~ 8.4 km). This
103 allows to resolve scales related to the first baroclinic mode, which is of the order of 30-40 km in the
104 GoM open-waters (e.g., Chelton et al., 1998). The model is forced with realistic open-boundary
105 conditions, high frequency atmospheric forcing, and freshwater and nutrient-rich discharges from
106 rivers. The analysis has been performed using 5-day averaged outputs for a period of 5 years from 2002
107 to 2007. We refer the reader to Damien et al. (2018) for an extended model and numerical setup
108 descriptions and a careful validation against observations that show the ability of the model to
109 reproduce the main hydrographic and nutrient vertical distributions in the GoM.



110 **Figure 1: 8-days composite images of $[CHL]_{surf}$ (in $mg \cdot m^{-3}$) around (a) May 29th 2003 and (b) October 19th 2004 derived from**
111 **Aqua-MODIS images overlaid with contours of Absolute Dynamic Topography (ADT in m) derived from Aviso images are**
112 **superimposed. Contour interval is 10cm and ADT values lower than 40cm are shown with dashed curves.**



113 **II.2/ Observational Data Set Used**

114 Satellite observations are used to evaluate the ability of GOLFO12-PISCES to reproduce the
115 dynamical and biological signatures associated with LCEs. Surface geostrophic velocities are derived
116 from a 1/4° multi-satellite merged product of absolute dynamic topography (ADT) provided by
117 AVISO+ (<http://marine.copernicus.eu>). Surface chlorophyll concentrations are from the Aqua-MODIS
118 4 km product (Sathyendranath et al., 2012; <http://marine.copernicus.eu>) and consist of 8-day
119 composites from 2003 to 2015.

120 **II.3/ LCEs detection, tracking and composite construction**

121 In order to track the LCEs, we use the algorithm developed by Nencioli et al. (2010), which has
122 been extensively employed to track coherent mesoscale eddies (Dong et al., 2012, Ciani et al. 2017,
123 Zhao et al. 2018) and submesoscale eddies (Damien et al., 2017). It is based on the geometric
124 organization of the velocity fields, dominated by rotation, that develop around eddy centers. Here, it is
125 applied to weekly AVISO+ surface geostrophic velocities and GOLFO12-PISCES 5-day averaged
126 velocities at 20m depth. Since LCEs are surface intensified (Cooper et al., 1990; Forristall et al., 1992;
127 Sturges and Kenyon, 2008), the choice of a shallow detection depth is expected to maximize the
128 accuracy. The selection of LCEs is defined using the criteria that eddies have to be shed from the Loop
129 Current.

130 In order to assess the [CHL] response to LCE dynamics, eddy-centric horizontal images and
131 transects of LCEs are used to make composites constructed by averaging modeled variables of the



132 different LCEs collocated to their center. The transect building procedure involves an axisymmetric
133 averaging that assumes axis-symmetry of the dynamical structures and no tilting of their rotation axis.
134 Moreover, we choose not to consider the LCEs formation period and the LCEs destruction period when
135 reaching the western basin (Lipphardt et al., 2008; Hamilton et al., 2018) as LCE destruction/formation
136 involves specific processes (Frolov et al., 2004; Donohue et al., 2016). We therefore focus on the LCEs
137 contained in the central part of the GoM from 86°W to 94°W. Annual composites are computed along
138 with monthly composite averages in order to assess seasonal variability. Composite LCEs averaged
139 during the months of January and February are referred to as winter composites and those averaged
140 during July and August are referred to as summer composites. These composites provide an overview
141 of the LCEs mean hydrographical, biogeochemical and dynamical characteristics.

142 **II.4/ Diagnostics**

143 The LCE radius R_{LCE} is estimated as the radial distance between the center and the peak
144 azimuthal velocity V_{max} . The mixed layer depth (MLD), a major physical factor influencing nutrient
145 distribution and [CHL] dynamics (Mann and Lazier, 2006), is defined as the depth at which potential
146 density exceeds its value at 10m depth by $0.125 \text{ kg}\cdot\text{m}^{-3}$ (Levitus, 1982; Monterey and Levitus, 1997).
147 An important driver of the mixed layer deepening is the stratification of the water column, which is
148 evaluated by the square of the buoyancy frequency $N^2(z) = \frac{-g}{\rho_0} \frac{\partial \rho}{\partial z}$, where g is the gravitational
149 acceleration, z is depth, ρ is density and ρ_0 is a reference density.

150 As carried out in Damien et al. (2018), several metrics are defined and used to describe [CHL]:



- 151 • $[CHL]_{surf}$: $[CHL]$ averaged between 0 and 30 m depth, and considered as surface concentration
- 152 (in $mg\ CHL \cdot m^{-3}$),
- 153 • $[CHL]_{tot}$: integrated content of $[CHL]$ over the 0-350 m layer (in $mg\ CHL \cdot m^{-2}$),
- 154 • DCM: depth of the Deep Chlorophyll maximum (in m),
- 155 • $[CHL]_{DCM}$: $[CHL]$ value at DCM depth (in $mg\ CHL \cdot m^{-3}$).

156 To understand the mesoscale distribution of $[CHL]$, key biological variables are vertically integrated
157 between 0 and 350m: the phytoplanktonic concentration $[PHY]_{tot}$, the primary production rate PP_{tot} and
158 the grazing rate GRZ_{tot} . PP_{tot} consists of two components: new production PPN_{tot} fueled by nutrients
159 supplied from a source external to the mixed layer and regenerated production PPR_{tot} sustained by
160 recycled nutrients within the euphotic layer (Dugdale & Goering, 1967; Eppley & Peterson, 1979). A
161 normalized chlorophyll concentration anomaly within LCEs, $[CHL]'$, is also computed as

162
$$[CHL]' = \frac{[CHL] - \overline{[CHL]}}{SD([CHL] - \overline{[CHL]})}$$
, where $\overline{[CHL]}$ is the averaged background $[CHL]$ field in the open

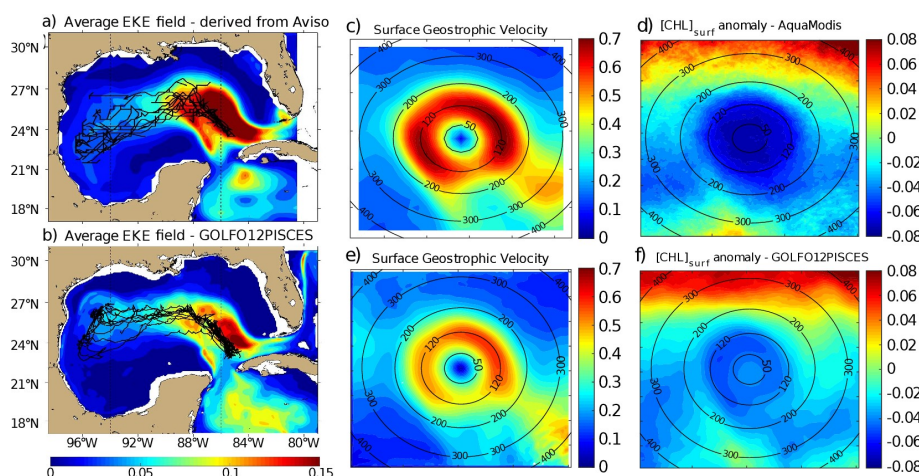
163 GoM waters (for radius > 250 km from the LCEs' centers) and SD the standard deviation operator,
164 following a similar approach as Gaube et al. (2013, 2014) and Dufois et al. (2016). To limit the
165 influence of very high $[CHL]$ values in coastal waters under the direct influence of continental
166 discharges, a salinity filtering criterion (lower than 36 psu) is applied. A similar method was used by
167 Gaube et al. (2013, 2014) to filter edge effects but using a distance criterion instead.

168 **III/ Results**

169 **III.1/ Satellite observations of $[CHL]$**



170 Fig 1 shows the 8-day averaged satellite observations of the surface chlorophyll around May 29th
171 2003 (a) and October 19th 2004 (b). These observations highlight the strong contrast between the
172 eutrophic conditions in the coastal waters and the oligotrophic conditions in the open ocean, as already
173 addressed by several studies (Martinez-Lopez & Zavala-Hidalgo, 2009; Pasqueron de Fommervault et
174 al., 2017). Far from the coast, these figures also reveal that the surface chlorophyll varies at a scale of
175 the order of 100km with a distribution that tends to follow the absolute dynamic topography (ADT)
176 contours.

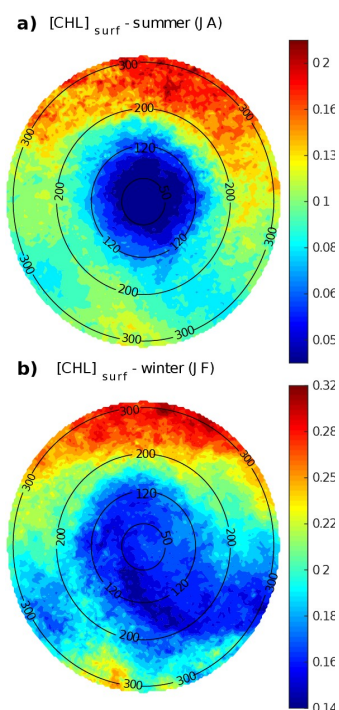


177 **Figure 2: Average eddy kinetic energy (EKE) field derived from (a) Aviso geostrophic surface velocities and from (b) GOLFO12-**
178 **PISCES currents at 10m depth. The trajectories of the tracked LCEs are superimposed to the EKE field (black lines). Vertical**
179 **black dashed lines indicate the central GoM area over which composites are built. Annual LCE composite images of surface**
180 **geostrophic velocities for (c) Aviso images and (e) GOLFO12-PISCES. Annual LCE composite images of surface chlorophyll**
181 **concentration anomaly for (d) Modis images and (f) GOLFO12-PISCES. Black circles indicate the radius in kilometers.**

182 LCEs trajectories are reported on Fig 2.a, superimposed onto the geostrophic climatological eddy
183 kinetic energy (EKE) field at the surface. EKE is computed from eddy velocities defined on each grid
184 cell as the difference between the total horizontal current and its mean value over 120 days. This time



185 window is chosen to filter the seasonal signal. EKE is concentrated in the LC and on the westward
186 pathway of the LCEs (Lipphardt et al. 2008) demonstrating that LCEs constitute the major source of
187 EKE in the GoM open waters (Sheinbaum et al., 2016; Sturges & Leben, 2000; Hamilton, 2007;
188 Jouanno et al., 2016).



189 **Figure 3: LCE composite images of $[\text{CHL}]_{\text{surf}}$ derived from Aqua-MODIS for the (a) summer and (b) winter seasons. Black circles**
190 **indicate the radius in kilometers.**

191 LCE annual composites of surface geostrophic velocities (Fig 2.c) and $[\text{CHL}]_{\text{surf}}$ (Fig 2.d) are
192 built from 482 different satellite images. On average, we found that $R_{\text{LCE}} \sim 120$ km and $V_{\text{max}} \sim 0.6\text{-}0.7$
193 $\text{m}\cdot\text{s}^{-1}$, in agreement with previously reported LCEs (Elliot, 1982; Cooper et al., 1990; Forristal et al.,
194 1992; Glenn and Ebbesmeyer, 1993; Weisberg and Liu, 2017; Tenreiro et al., 2018). LCEs are
195 associated with a negative $[\text{CHL}]_{\text{surf}}$ anomaly (~ -0.07 $\text{mg}\cdot\text{m}^{-3}$ in the annual average). The LCEs



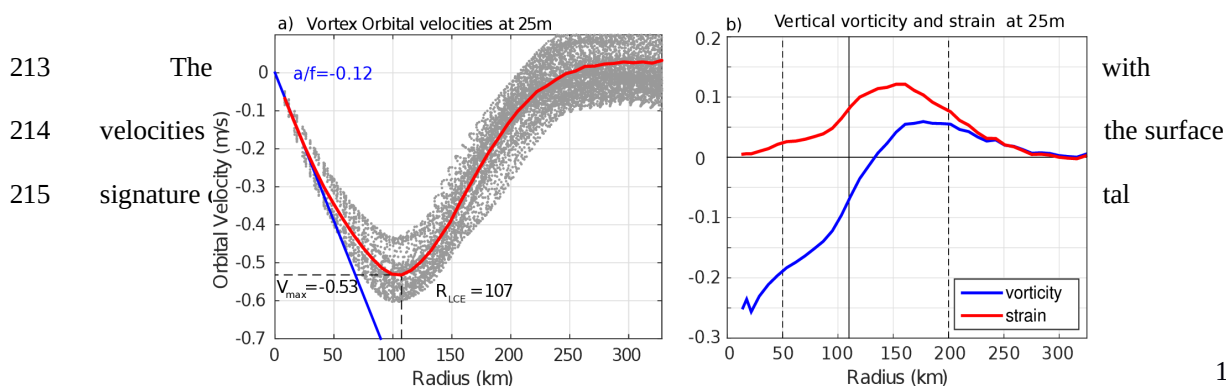
196 influence on $[\text{CHL}]_{\text{surf}}$ is largest in summer (Fig 3.a) when it reaches very low values ($< 0.045 \text{ mg}\cdot\text{m}^{-3}$),
197 which corresponds to an anomaly of $\sim -0.08 \text{ mg}\cdot\text{m}^{-3}$. This anomaly is less marked in winter (~ -0.06
198 $\text{mg}\cdot\text{m}^{-3}$, Fig 3.b) when $[\text{CHL}]_{\text{surf}} \sim 0.17 \text{ mg}\cdot\text{m}^{-3}$ within LCEs. The high chlorophyll concentrations in the
199 northern part of the composites (in the southern part too but in smaller proportions) are related to
200 shelves.

201 III.2/ Dynamical characterization of modeled LCEs

202 A total of 11 model LCEs were detected during the 5 years of simulation. Their trajectories are
203 reported in Fig 2.b, superimposed upon the climatological EKE field simulated at 10 meters. The
204 westward / southwestward propagation of LCEs is well reproduced (Vukovich, 2007) even though the
205 LCEs translation is almost zonal in GOLFO12-PISCES. Comparison with Fig 2.a shows the ability of
206 GOLFO12-PISCES to represent the mean and transient dynamical features of the GoM open waters
207 (see also Garcia-Jove et al., 2016).

208 The robustness of the composite method arises from the number of LCE images used to build the
209 composites:

- 210 • Annual composite is built from 605 5-day averaged LCE pictures from 10 different LCEs,
- 211 • Summer composite is built from 83 5-day averaged LCE pictures from 8 different LCEs,
- 212 • Winter composite is built from 93 5-day averaged LCE pictures from 9 different LCEs.





216 velocities ($\sim 25\%$ on average over the 50-200 km radius range). This bias could result from the
217 relatively coarse model resolution and 5-day output frequency that are unable to fully capture the
218 gradient intensity at R_{LCE} . The assumption of an axial symmetry of the LCE circulation around its
219 center also induces an error that tends to decrease V_{max} .

220 **Figure 4: (a) Orbital velocities at 25m depth in function of the radius of each detected LCE (light gray dots). The red line is the**
221 **LCE orbital velocity profile of the annually-averaged composite. (b) Vertical vorticity and strain computed from the averaged**

222 **orbital velocity profile assuming no radial velocity in cylindrical coordinates as** $\zeta_z = \frac{1}{fr} \frac{\partial rv}{\partial r}$ **and** $S = \frac{1}{f} \left(\frac{\partial v}{\partial r} - \frac{v}{r} \right)$.

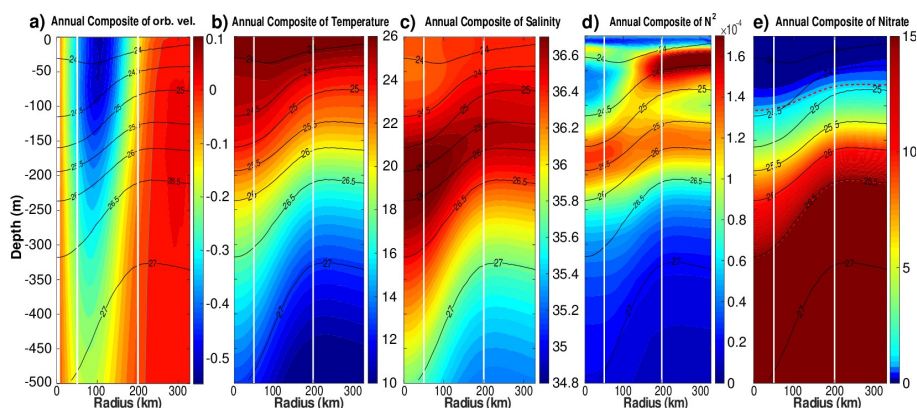
223 Orbital velocities of composite eddies are used to distinguish different dynamical areas within
224 LCEs. The model annual average dynamical profile at 25m depth (Fig 4) reveals a typical vortex-like
225 structure with $R_{LCE} \sim 107$ km and $V_{max} \sim 0.53$ m·s⁻¹ and suggests the following decomposition:

- 226 • $r < 50$ km : the **LCEs core**, where the eddy is approximately in solid body rotation: $V_{orb} = a \cdot r$
227 where the coefficient a is related to the Rossby number ($Ro = 2a/f$). The ratio a/f is estimated
228 to be ~ -0.12 (Fig. 4). In this field, the strain is reduced to a minimum and the flow is dominated
229 by rotation.
- 230 • 50 km $< r < 200$ km: the **LCEs ring** structure where the orbital velocity reaches its maximum
231 at R_{LCE} and then decreases. The horizontal strain is important in this field, even dominating
232 vorticity from radius exceeding R_{LCE} .
- 233 • $R > 200$ km: the **background GoM**, where the velocity anomalies related to the LCE vanish.

234 In the vertical (Fig 5.a), LCEs are near-surface intensified anticyclonic vortex rings. At depth,
235 the orbital peak velocity decreases rapidly. At 500 m depth, $V_{max} \sim 0.17$ m·s⁻¹ and $R_{LCE} \sim 75$ km, and



236 the dynamical LCE signal nearly vanishes below 1500 m depth ($V_{\max} < 0.03 \text{ m}\cdot\text{s}^{-1}$). The proposed
237 division into 3 distinct dynamical regions applies from the surface down to 500 m depth (Fig 5.a).



238 **Figure 5: Annually-averaged LCE composite transects of (a) orbital velocities [m/s], (b) potential temperature [°C], (c) salinity**
239 **[psu], (d) squared Brunt-Väisälä frequency (N^2 in s^{-2}) and (e) nitrate concentration [$\text{mmol}\cdot\text{m}^{-3}$]. Isopycnals anomalies (black**
240 **contours) are superimposed on all panels. Vertical white lines delimit the three dynamical fields of the LCE composite. On panel**
241 **e, dashed red lines highlights two specific iso-nitrate contours: 1 and 15 $\text{mmol}\cdot\text{m}^{-3}$.**

242 The composite hydrological structure of modeled LCEs is shown in Fig 5.b and 5.c. The
243 depression of isopycnals, associated with a depression of isotherms and isohalines, is characteristic of
244 oceanic anticyclones. In the core of the eddies, the composite depicts a salinity maximum located
245 between 100 and 300 m, corresponding to the signature of the Atlantic Subtropical UnderWater
246 (ASTUW) of Caribbean origin entering the GoM through the Yucatan Channel (Badan et al., 2005;
247 Hernandez-Guerra & Joyce, 2000; Wuust, 1964). This salinity maximum is not limited to the core of
248 the LCE but gradually erodes and shallows: 36.82 psu at 200 m in the LCEs core and 36.61 psu at 150
249 m in the background GoM common water. Details on the fate of this salinity maximum investigated
250 with GOLFO12 simulations can be found in Sosa-Gutiérrez et al. (2020). The ASTUW layer (salinity >
251 36.5 psu) is also thicker in the LCEs core (~190 m thick) compared to the background GoM water

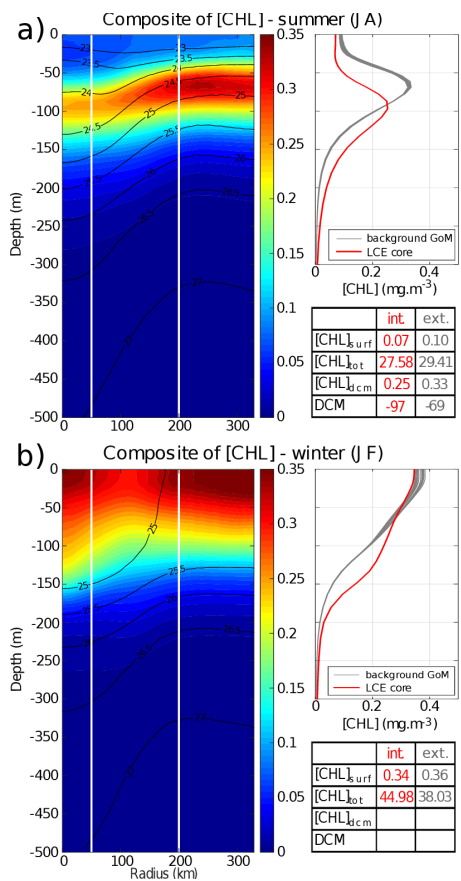


252 (~120 m thick). Overall, GOLFO12-PISCES reproduces the observed hydrological structure of LCEs
253 (Elliott, 1982; LeHenaff et al., 2012; Hamilton et al., 2018; Meunier et al., 2018b).

254 The annually averaged LCE composite presents a lens-shaped structure exhibiting a ~50 m thick
255 layer of weakly stratified waters located between 50 and 100 m depth (Fig 5.d). This subsurface modal
256 water presents hydrological characteristics close to the observed background GoM waters (potential
257 temperature ~25.4°C and salinity ~ 36.3 psu, Meunier et al., 2018b) and is surrounded below and above
258 by well stratified layers (Meunier et al., 2018a). The upper pycnocline varies seasonally and vanishes in
259 winter due to the deepening of the mixed layer, whereas the lower pycnocline is permanent.

260 The downward displacement of isopycnals is associated with a depletion of nutrients in the upper
261 layer of the LCEs core (Fig 5.e). This is a typical feature of mesoscale anticyclones in the ocean
262 (McGillicuddy et al. 1998; Oschlies and Garcon, 1998). The $1 \text{ mmol}\cdot\text{m}^{-3}$ iso-nitrate concentration
263 (hereafter Z_{NO_3} , sometimes referred to as the nitracline as in Cullen & Eppley, 1981; Pasqueron de
264 Fommervault et al., 2017 or Damien et al., 2018) is located at ~ 70 m depth in the background GoM
265 waters whereas it is found much deeper in the core ($Z_{\text{NO}_3} \sim 106 \text{ m}$). At depth, iso-nitrate layers and
266 isopycnals are well correlated (Ascani et al., 2013; Omand & Mahadevan, 2014). For instance, iso-
267 nitrate concentration of $15 \text{ mmol}\cdot\text{m}^{-3}$ follows the displacements of the $1026.5 \text{ kg}\cdot\text{m}^{-3}$ isopycnal.
268 However, above 150 m, the density/nitrate relation is different inside and outside the eddies (Z_{NO_3} is
269 collocated with isopycnal $1024.4 \text{ kg}\cdot\text{m}^{-3}$ in the LCEs core while it is on isopycnal $1024.9 \text{ kg}\cdot\text{m}^{-3}$ in the
270 background GoM).

271 **III.3/ Surface and vertical distribution of chlorophyll in LCEs**



272 **Figure 6: LCE composite transects of [CHL] during summer season (A) and winter season (B). Density anomalies (black**
 273 **contours) are superimposed. Vertical white lines delimit the three dynamical fields of the LCE composite. For each season, [CHL]**
 274 **profiles in the LCE core ($r < 50$ km, red lines) and in the background GoM ($200 \text{ km} < r < 330$ km, gray lines) are plotted. Key**
 275 **metrics concerning [CHL] profiles are also indicated in the tables.**

276 The large difference in stratification between the LCEs core and background GoM suggests a
 277 contrasted seasonal response of the [CHL]. This is confirmed by the analysis of summer and winter
 278 composites of [CHL] vertical distribution:

- 279 • In summer (Fig 6.a), [CHL]_{surf} is ~ 30% lower in the LCEs core ($r < 50$ km) than in the
 280 background GoM ($200 \text{ km} < r < 330$ km). A pronounced DCM, characteristic of oligotrophic
 281 environments, is deeper in the core (~ 97 m) than in the background GoM (~ 69 m) with
 282 chlorophyll concentrations significantly lower in the interior (~ - 25%).

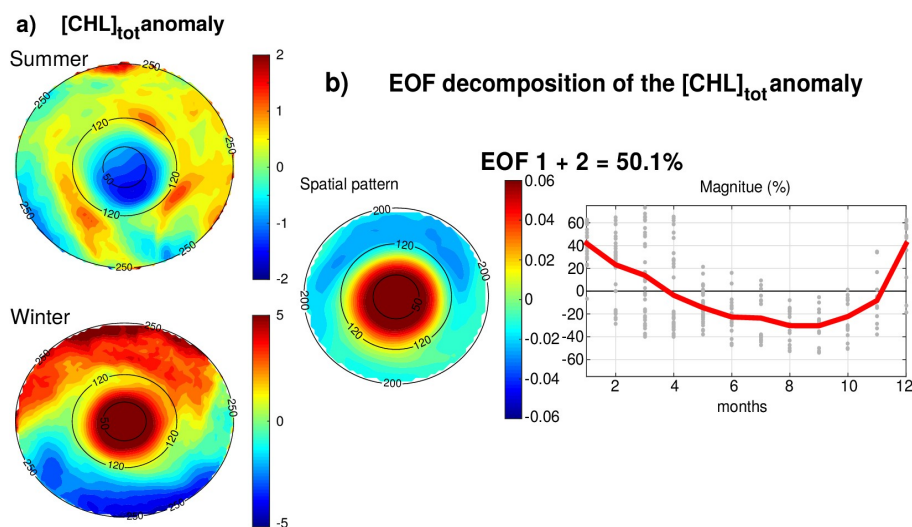


283 • In winter, the [CHL] is maximum at the surface in all the composite domains (Fig 6.b).
284 [CHL]_{surf} is lower in the LCEs core compared to the background GoM but the difference is less
285 marked (~ - 6%) than in summer. The main discrepancy is the depth of the inflection point of
286 these profiles. It is deeper in the LCEs core (~-150 m), resulting in a more homogenized [CHL]
287 over a deeper layer than in the background GoM (~-120 m).

288 However, despite reduced surface concentration both in winter and summer, the integrated
289 chlorophyll content, [CHL]_{tot}, shows a distinct seasonal pattern compared to the surface (tables in Fig
290 6):

- 291 • In summer, [CHL]_{tot} is lower in the LCEs core (27.58 mg·m⁻²) compared to the background
292 GoM (29.41 mg·m⁻²) and $\Delta[\text{CHL}]_{\text{tot}} = -1.83 \text{ mg}\cdot\text{m}^{-2}$,
- 293 • In winter, [CHL]_{tot} is higher in the LCEs core (44.98 mg·m⁻²) compared to the background GoM
294 (38.03 mg·m⁻²) and $\Delta[\text{CHL}]_{\text{tot}} = + 6.95 \text{ mg}\cdot\text{m}^{-2}$.

295 The winter increase of [CHL]_{tot} is around 29% in the background GoM whereas it reaches 63% in the
296 LCEs core, leading to [CHL]_{tot} in the core being larger than [CHL]_{tot} in the background GoM in winter.
297 Meanwhile, [CHL]_{surf} remains lower within the LCEs core. The fact that the [CHL] at the surface does
298 not reflect its depth-integrated behavior means that the peculiar variability of [CHL] within LCEs may
299 not be fully captured by ocean color satellite measurements. This is consistent with Pasqueron de
300 Fommervault et al. (2017) and Damien et al. (2018) observations and modeling results which addressed
301 the vertical [CHL] distribution in the GoM.

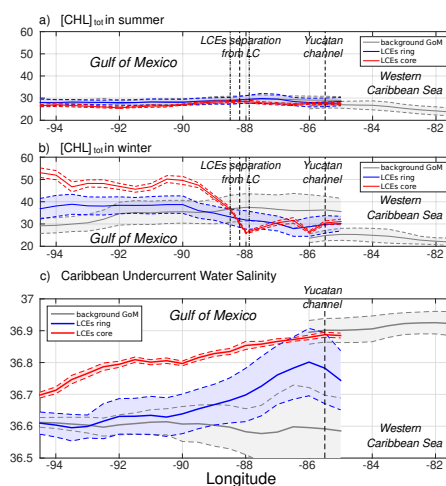


302 **Figure 7: (a) Anomaly of $[\text{CHL}]_{\text{tot}}$ in summer and winter seasons. Black circles indicate the radius in kilometers. (b) EOF**
303 **decomposition of the $[\text{CHL}]_{\text{tot}}$ anomaly. The spatial patterns and monthly magnitude (gray dots; the red line represents their**
304 **monthly averaged value) of the two first modes are indicated. Modes 1 and 2 were summed together (upper panel) and represent**
305 **50.1% of the total variance.**

306 $[\text{CHL}]_{\text{tot}}$ is strongly shaped by both the seasonal variability and the LCEs. The seasonal
307 composites of $[\text{CHL}]_{\text{tot}}$, shown in Fig 7.a, confirm the summer/winter contrast and highlight a
308 monopole structure with a relatively homogeneous distribution of $[\text{CHL}]_{\text{tot}}$ within the eddy's core. In
309 order to better characterize the spatio-temporal variability of $[\text{CHL}]_{\text{tot}}$ induced by LCEs, an Empirical
310 Orthogonal Function (EOF) analysis was performed on the $[\text{CHL}]_{\text{tot}}$ anomaly (Fig 7.b) following the
311 methodology of Dufois et al. (2016). It consists in decomposing the signal into orthogonal modes of
312 variability. Here, we have chosen to focus on the first two most significant modes which explain 40.2%
313 and 9.9% of the variability. Since they both depict a similar monopole structure in the LCEs core, they
314 were added up in a mode referred to EOF 1+2 responsible for 50% of the total $[\text{CHL}]_{\text{tot}}$ variance within
315 LCEs. The third eigenmode (not shown) accounts for 6.2% and depicts a dipole structure with opposite
316 polarity located at the east and north of the eddy center. On average, the EOF1+2 mode is positive in



317 winter (from December to March) and negative the rest of the year (from April to November), with a
318 maximum in January December and a minimum in September. This justifies, a posteriori, the choice to
319 consider winter and summer LCE composites.



320 **Figure 8: (a) Summer $[CHL]_{tot}$, (b) winter $[CHL]_{tot}$ and (c) salinity of Caribbean waters (ASTUW defined as the subsurface**
321 **salinity maximum) as a function of longitude in (red) the LCEs core, (blue) the LCEs ring and in (gray) the background GoM.**
322 **Full lines indicate the averaged value and dashed lines the +/- one standard deviation interval.**

323 The composite evolution of the LCEs $[CHL]_{tot}$ along their westward journey is shown in Fig 8.a
324 and 8.b. It illustrates how the total chlorophyll concentration is preferentially increased in winter within
325 the LCEs core, as soon as the LCEs are shed from the LC. The winter $[CHL]_{tot}$ within LCEs is much
326 larger (exceeding one standard deviation) than the background winter $[CHL]_{tot}$. In terms of integrated
327 $[CHL]$, the LCEs-induced seasonal variability overwhelms the GoM open-waters background seasonal
328 variability.

329 **IV/ Discussion**



330 In an oligotrophic environment such as the GoM open-waters, the primary production is
331 generally limited by nutrient supply and $[\text{CHL}]_{\text{tot}}$ exhibits low seasonal variability at the GoM basin
332 scale (Pasqueron de Fommervault et al., 2017). The winter increase of $[\text{CHL}]_{\text{tot}}$ within the LCEs core
333 (which translates into an effective increase of biomass, see appendix A) contrasts and may have large
334 implications for the regional biogeochemical cycles and ecosystem structuration. It also echoes several
335 studies which report elevated $[\text{CHL}]_{\text{surf}}$ within anticyclonic eddies in the oligotrophic subtropical gyre
336 of the southeastern Indian Ocean (Martin and Richards, 2001; Waite et al., 2007; Gaube et al., 2013;
337 Dufois et al., 2016, 2017; He et al., 2017), questioning the classical paradigm of low productivity
338 usually associated with anticyclonic eddies.

339 The mechanisms explaining the LCE impact on $[\text{CHL}]$ are discussed below, trying to rationalize
340 the respective role of abiotic (e.g., trapping, winter mixing, Ekman pumping) and biotic processes (e.g.,
341 primary production (PP), grazing pressure, regenerated versus new PP).

342 **IV.1 Eddy trapping**

343 The distinct hydrological and biogeochemical properties associated with the LCEs core suggest
344 their ability to trap and transport oceanic properties. This mechanism, known as the eddy-trapping
345 (Early et al., 2011; Lehahn et al., 2011; McGillicuddy, 2015; Gaube et al., 2017) is efficient only if the
346 orbital velocities of the vortex are faster than the eddy propagation speed (Flierl, 1981; d'Ovidio et al.,
347 2013). The rotational velocities of the model LCEs are $\sim 0.53\text{m}\cdot\text{s}^{-1}$ are one order of magnitude larger
348 than the propagation velocities ($\sim 0.046\text{m}\cdot\text{s}^{-1}$ on average). This suggests that LCEs might have a



349 certain ability to trap the water masses present in their core with relatively low exchanges with the
350 exterior.

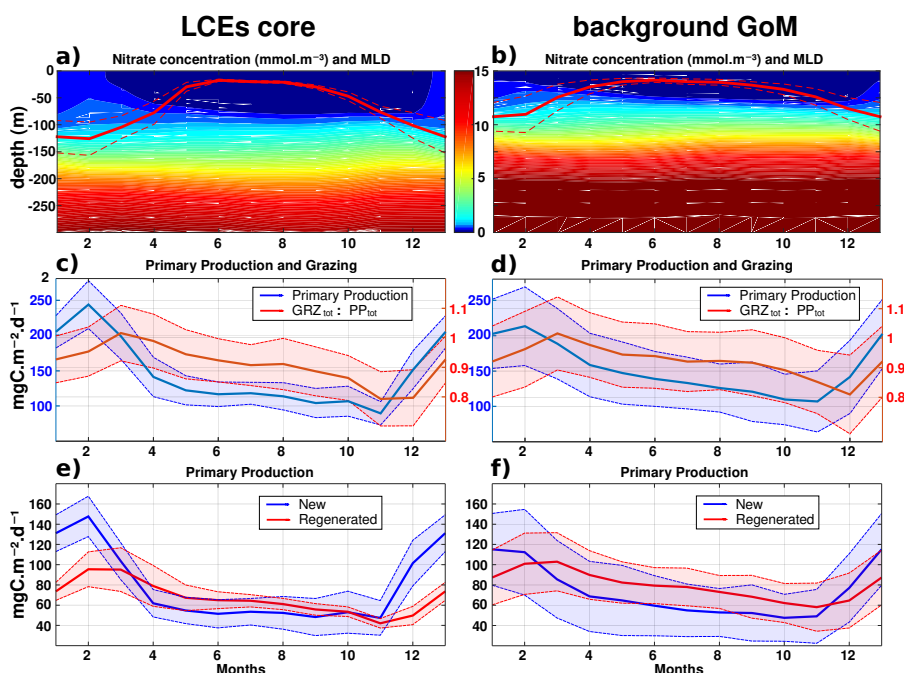
351 Salinity is well-suited to investigate water masses trapped within the LCEs core during their
352 propagation toward the western GoM (Fig 8.c; Sosa-Gutierrez et al., 2020): salinity distribution shows a
353 marked subsurface maximum that it is not affected by biogeochemical processes. In the Western
354 Caribbean Sea, ASTUW is characterized by high salinity (~ 36.9 psu on average) and low standard
355 deviation (< 0.05 psu). The eastern GoM salinity field reveals that most of the ASTUW crosses the
356 Yucatan Channel within the Loop Current. During the formation of LCEs, a significant part of
357 ASTUW is captured into the LCEs core with low alteration of its properties (Fig 5.c and 8.c). Within
358 the LCEs core, the water mass is transported from eastern to the western GoM where its salinity
359 decreases from 36.9 psu to 36.7 psu. Although altered, the ASTUW signature is still clearly detectable
360 in the GoM western boundary. The other part of ASTUW entering the GoM is found in the LCEs ring.
361 Compared to the core, the salinity in the ring is on average lower (~ 36.8 psu in the eastern GoM) and
362 presents a high standard deviation, pointing out that more recent ASTUW co-exists with older ASTUW
363 that yields eroded salinity maxima. As LCEs travel westward across the GoM, salinity in the LCEs ring
364 decays rapidly to reach values similar to the background GoM values (~ 36.6 psu). This
365 homogenization mainly arises from vertical mixing and winter mixed layer convection (Sosa-Gutierrez
366 et al., 2020). Horizontal intrusions and filamentation may also contribute to this homogenization
367 (Meunier et al., 2020). The composites also suggest that almost no ASTUW enters the GoM apart from
368 the LCEs. The slight increase of the background salinity from eastern to western GoM is a consequence
369 of the diffusion of salt from the LCEs toward the exterior.

370 Although LCEs undergo considerable decaying rates, their erosion is particularly strong in the
371 ring while the core remains better isolated from the surrounding waters (Lehahn et al., 2011; Bracco et



372 al., 2017). Given that the LCEs core is also quite homogeneous, the following discussion relies on the
373 analysis of the seasonal cycles of selected parameters averaged within the LCEs core.

374 IV.2 Nitracline depth and nutrient supply into the mixed layer



375 **Figure 9:** Climatological seasonal cycles of (a and b) nitrate concentration profiles (the red line overlaid is the average mixed layer
376 depth), (c and d) the total primary production (blue) and the ratio of grazing rate over primary production (red) and (e and f) the
377 new (blue) and regenerated (red) primary production. The left panels (a, c and e) refer to the seasonal time series in the LCEs
378 core ($r < 50$ km) whereas the right panels (b, d and f) refer to the seasonal time series in the background GoM ($r > 200$ km). For
379 each average cycle, the mean value is shown (full line) along with its variability (± 1 standard deviation relative to the mean,
380 dashed lines).

381 The LCEs impact the upper ocean stratification (Fig 5.d), the nutricline depth (Fig 5.e) and
382 consequently the nutrient supply to the euphotic layer (McGillicuddy et al., 2015). The relationship



383 between mixed layer deepening and nutrient supply is studied here by comparing the Z_{NO_3} with the
384 MLD (Fig 9.a,b).

385 In late-spring and summer (from May to September), the water column is stratified (shallow
386 MLD) and the downward displacement of the isopycnals within the LCEs pushes nutrients below the
387 euphotic zone (see also Figs 5.e, 6.a): less nutrients are available within the LCE cores for
388 phytoplankton growth, explaining a deeper and less intense DCM. In winter, the convective mixing,
389 fostered both by intense buoyancy losses and strong mechanical energy input at the surface, causes a
390 larger deepening of the mixed layer within the LCEs core (\sim - 125 m, Fig 9.a) compared to the
391 background (\sim - 85 m, Fig 9.b). This asymmetry is due to a pronounced decrease of the surface and
392 subsurface stratification within the LCE core (Fig 5.d, Kouketsu et al., 2012). A quantitative diagnostic

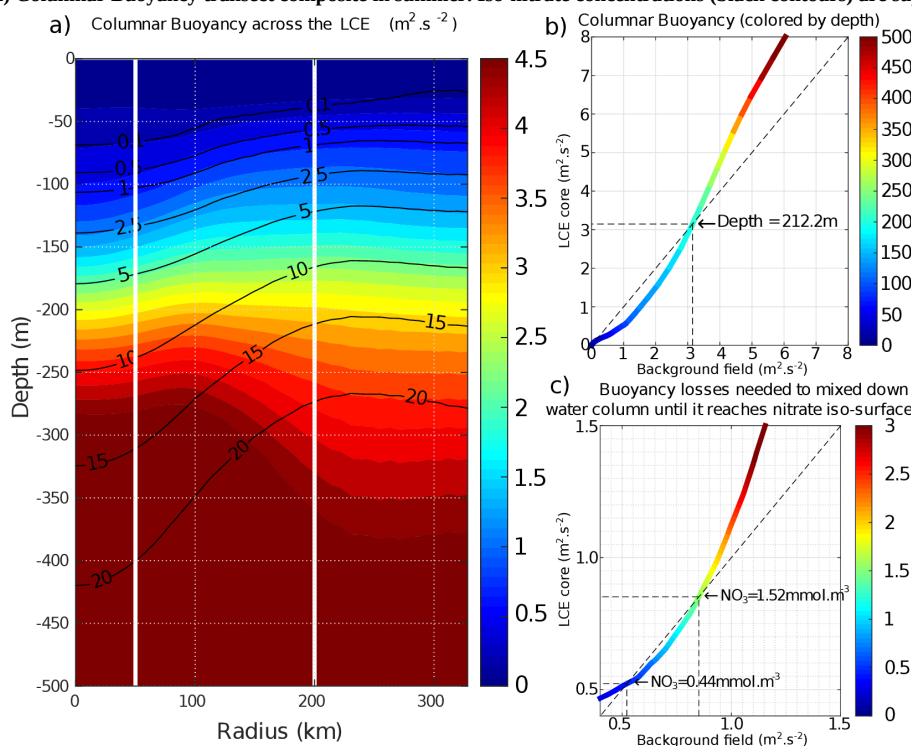
393 of the stratification is given by the columnar buoyancy, $\int_0^H N^2(z) \cdot z \cdot dz$ which measures the buoyancy
394 loss required to mix the water column to a depth H (Herrmann et al. 2008). Fig 10.a reveals significant
395 differences in pre-winter buoyancy between the eddy core and its surroundings. Assuming that the
396 change in buoyancy content is mainly controlled by the buoyancy flux at the surface (see Turner 1973;
397 Lascaratos & Nittis, 1998), it suggests that mixing the water column down to \sim -210 m depth requires
398 smaller surface buoyancy loss in LCEs cores compared to the background GoM (Fig 10.b).

399 However, the larger winter deepening of the mixed layer within the LCEs core is not a sufficient
400 condition to explain a larger nutrient supply. Indeed, it fosters the transport of nutrients from the
401 nitracline toward the mixed layer because both are getting closer. Fig 10.c highlights that a smaller
402 buoyancy loss mixes down the water column to greater nutrient concentration levels in the LCEs core
403 compared to the LCEs surrounding. This likely explains the winter increase of surface nitrate



404 concentration within the LCEs (Fig 9.a). In addition, a diagnostic of the different contributions to
405 $[\text{NO}_3]$ evolution is proposed in appendix B. It shows the dominant role of vertical advection and
406 diffusion in winter in providing nutrients to the euphotic layer in the LCEs core.

407 **Figure 10: (a) Columnar Buoyancy transect composite in summer. Iso-nitrate concentrations (black contours) are superimposed.**



408 Vertical white lines delimit the three dynamical fields of the LCE composite. (b) Vertical increase of the columnar buoyancy in
409 the LCEs core versus the background GoM. Colors refer to depth. (c) Columnar buoyancy loss required to mix the water column
410 down to the iso-nitrate surface defined by the line color.

411 So far we have assumed that the surface buoyancy fluxes are identical over the LCEs core and
412 the background GoM. However, this is not strictly the case because temperature/salinity features in the
413 LCEs and background waters are different (Fig 5.b,c; see also Williams 1988). The modeled surface
414 buoyancy loss during winter season is $\sim 18\%$ more intense within the LCEs. This difference is
415 substantial and probably mainly driven by additional surface cooling applied on the warm LCE core



416 through air-sea interaction. It contributes to enhance convection within the eddies core, and then
417 nutrient supply toward the surface.

418 **IV.3 Productivity**

419 The primary productivity PP_{tot} presents a clear seasonal cycle both in the LCEs cores and in the
420 background GoM with lower values in October-November, a sharp increase starting in November, a
421 maximum in February and a gradual decrease from March to October (Fig 9.c and 9.d). The pressure
422 exerted by zooplankton grazers varies seasonally. It shows a similar seasonal cycle in the LCEs core
423 and in the background GoM. On average, ~ 90% of the total daily growth is consumed by grazing,
424 reaching the highest impact in March, just one month after the peak season of the PP_{tot} in both LCEs
425 dynamical areas. The annual PP_{tot} is slightly lower in the LCEs core (~ 142.4 $mgC \cdot m^{-2} \cdot d^{-1}$) than in the
426 background GoM (~ 148.9 $mgC \cdot m^{-2} \cdot d^{-1}$). The amplitude of the seasonal cycle is larger in the LCEs
427 core: from April to November, PP_{tot} is on average ~12% lower in the LCEs core whereas, in winter,
428 PP_{tot} is ~14% higher where it reaches ~ 243.2 $mgC \cdot m^{-2} \cdot d^{-1}$ in February.

429 The ratio of the PPN_{tot} and PPR_{tot} provides information about the mechanisms controlling the
430 biomass growth (Fig 9.e and 9.f). In winter, the PPN_{tot} plays a leading role, reaching up to 113-147
431 $mgC \cdot m^{-2} \cdot d^{-1}$, driven by the winter mixing and induced NO_3 fluxes (see Appendix B). Conversely, the
432 PPR_{tot} is dominant from April to October. During this period, low NO_3 resources are available in the
433 euphotic layer and the ecosystem preferentially uses ammonium to sustain the PP_{tot} . This seasonal
434 pattern is characteristic of oligotrophic environments such as the GoM open waters (Wawrik et al.,
435 2004; Linacre et al., 2015).



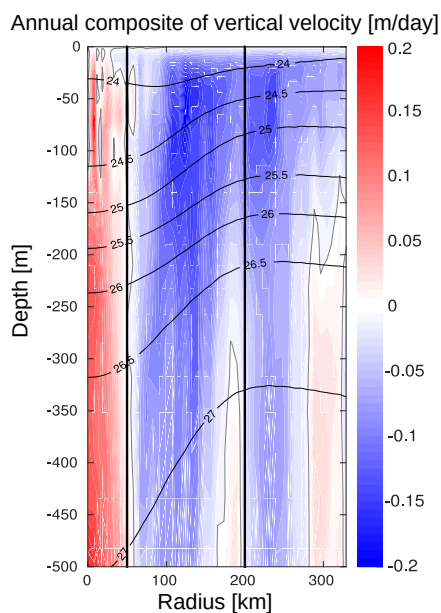
436 In winter, changes in PP_{tot} are correlated to the intensity of winter mixing in the LCEs core (Fig
437 9.c) and the background GoM (Fig 9.d). The larger PPN_{tot} in the eddy core is consistent with a larger
438 supply of NO_3 and evidences that the core of anticyclones can be preferential spots of enhanced
439 biological production.

440 **IV.4 How to explain summer productivity?**

441 In summer, the total primary production is higher in the background GoM waters as the
442 regenerated production rate is higher. But surprisingly, the new primary production exhibits similar
443 rates in both regions, although NO_3 depletion occurs deeper in the LCEs core. In the absence of a
444 strong enough vertical mixing when the mixed layer is shallow, this apparent mismatch requires an
445 additional mechanism, vertical advection, capable to supply NO_3 to the euphotic layer (Sweeney et al.,
446 2003; McGillicuddy et al., 2015).

447 The model vertical velocity in the LCEs reveals an upward pumping in their core (Fig 11). The
448 vertical velocity between 100 and 500 m is on average $+0.07 \text{ m}\cdot\text{day}^{-1}$. This vertical transport is mainly
449 driven by two mechanisms, eddy pumping (Falkowski et al., 1991) and eddy-wind interaction (Dewar
450 and Flierl, 1987), but their relative importance is difficult to quantify (Gaube et al. 2014; McGillicuddy
451 et al., 2015).

452 The eddy pumping mechanism is related to the decay of the rotational velocities from the
453 moment LCEs are released from the Loop Current. In the LCE core, this decay is considered as
454 moderate since lateral diffusivity is expected to be relatively low (section V.1). This process may
455 however be considerable in the LCE ring where the erosion rates are important (Meunier et al., 2020).



456 **Figure 11: Annually-averaged LCE composite transects of vertical velocities (m/day). Isopycnals anomalies (black contours) are**
457 **superimposed on all panels. Vertical white lines delimit the three dynamical fields of the LCE composite.**

458 Eddy-wind interactions are due to mesoscale modulation of the Ekman transport. Following the
459 observation of a LCE core in quasi-solid body rotation, the horizontal vorticity varies little with the
460 radius resulting in a negligible “non-linear” contribution of the Ekman pumping (McGillicuddy et al.,
461 2008; Gaube et al., 2015). Assuming a small effect of the eddy SST-induced Ekman pumping, the total

462 Ekman pumping simplifies into its “linear” contribution computed as $W_E = \frac{\nabla \times \tau}{\rho_0 \cdot (f + \zeta)}$, where ρ_0 is the

463 surface density, f the Coriolis parameter, τ the stress at the sea surface depending on both the wind and
464 ocean currents at the surface (Martin and Richards, 2001, equation 12) and $\nabla \times$ the curl operator.

465 Considering uniform wind velocities ranging from 4.5 to 7.5 m·s⁻¹ (Nowlin & Parker, 1974;

466 Passalacqua et al., 2016) blowing over the LCE, the curl of the stress arises from the anticyclonic



467 surface circulation generated by the eddy. Its manifestation is a persistent horizontal divergence at
468 surface balanced by an upward pumping in the eddy interior (see Martin & Richards, 2001; Gaube et
469 al., 2013, 2014 for further details). With $\rho_0 \sim 1023 \text{ kg}\cdot\text{m}^{-3}$ and $f \sim 6.2\cdot 10^{-5} \text{ s}^{-1}$, we estimate W_E to be in
470 the order of $+ 0.06\text{-}0.13 \text{ m}\cdot\text{day}^{-1}$, in agreement with the modeled vertical velocity within the core. The
471 Ekman-eddy pumping mechanism could explain a large fraction of the gradual upwelling of isopycnals
472 within the eddy's core and may actively contribute to the advective vertical flux of nutrients (see
473 Appendix B). In summer, this mechanism could explain why new primary production rates are similar
474 in the LCEs core and the background GoM waters although the nutrient pool is located much deeper in
475 the LCEs core.

476 The eddy-Ekman pumping persists in the LCEs core throughout their lifetime as long as there is
477 a wind stress applied at the surface. During wintertime, we expect that both vertical mixing and eddy-
478 Ekman pumping participate to increase the new primary production. A question then arises on the
479 relative contribution of winter mixing to eddy-Ekman pumping in the LCEs core primary production
480 increase in winter. This issue was tackled by He et al. (2017) and Travis et al. (2019) comparing the
481 rate of change of the mixed layer depth with the vertical velocity induced by the eddy-Ekman pumping
482 (equation 4 in He et al, 2017). In the LCEs core, we estimate the mixed layer to deepen at roughly 0.8
483 $\text{m}\cdot\text{day}^{-1}$, which is on average about 10 times larger than pumping mechanism. This supports winter
484 mixing as the overwhelming process for the LCEs-induced primary production peak in winter.

485 **V/ Summary and perspectives**

486 The [CHL] variability induced by the mesoscale Loop Current Eddies in the Gulf of Mexico is
487 studied by analyzing vortex composite fields generated from a coupled physical-biogeochemical model



488 at 1/12° horizontal resolution. LCEs are hotspots for mesoscale biogeochemical variability. Despite the
489 $[\text{CHL}]_{\text{surf}}$ negative anomaly associated with their core ($r < 50$ km), model results indicate that LCEs are
490 associated with enhanced phytoplankton biomass content, particularly in winter. This enhancement
491 results from the contribution of multiple mechanisms of physical-biogeochemical interactions and
492 contrasts with the background oligotrophic surface waters of the GoM.

493 The main results of this study are:

- 494 • LCEs cores present a negative surface chlorophyll anomaly,
- 495 • Unlike $[\text{CHL}]_{\text{surf}}$, $[\text{CHL}]_{\text{tot}}$ is larger in the LCEs cores compared to the background GoM in
496 winter.
- 497 • LCEs core trigger a large phytoplankton biomass increase in winter,
- 498 • The winter mixing is a key mesoscale mechanism that preferentially supplies nutrients to the
499 euphotic layer within the LCEs core. Consequently, it drives an eddy-induced peak of new
500 primary production,
- 501 • Ekman-eddy pumping is a significant mechanism for sustaining relatively high new primary
502 production rates within LCE cores during summer.

503 The phytoplankton biomass increase in individual LCEs cores suggests that LCEs play an important
504 role in sustaining the large-scale GoM productivity.

505 Although the biological response to LCEs may present some specificities due to the particular
506 dynamical nature of LCEs, this study suggests potentially generic insights on the biogeochemical role
507 that anticyclonic eddies could play in oligotrophic environments. It echoes the previous works of
508 Martin and Richards (2001), Gaube et al. (2014, 2015) and especially Dufois et al. (2014, 2016) and He
509 et al. (2017) who proposed winter vertical mixing as an explanation for the positive $[\text{CHL}]_{\text{surf}}$ anomaly
510 observed in anticyclones in the South Indian Ocean. One of the most crucial points to be underlined



511 from our results is that the enhanced primary production and biomass content within anticyclonic
512 eddies may not necessarily be correlated with the surface layer variability. In oligotrophic areas, the
513 integrated content of chlorophyll in the water column has to be considered. This implies that caution
514 should be exercised in the analysis and interpretation of $[\text{CHL}]_{\text{surf}}$ observed by remote sensing
515 instruments and highlights the crucial need for in-situ biogeochemical and bio-optical measurements.
516 In oligotrophic environments, defined by their low production rates and their low chlorophyll
517 concentration, anticyclonic eddies are able to trigger local enhanced biological productivity and
518 generate phytoplankton biomass positive anomalies. In a scenario of expansion of oligotrophic areas
519 (Barnett et al., 2001; Behrenfeld et al., 2006; Polovina et al., 2008), the fate and role of mesoscale
520 anticyclones is an important aspect to be considered.

521 This study focuses on mesoscale physical-biogeochemical interactions which is the spectral
522 range resolved by GOLFO12-PISCES configuration. To go further into the analysis of anticyclonic
523 eddies in oligotrophic environments, the role of submesoscale is of particular interest since it has been
524 proved to trigger mechanisms of significance importance for biogeochemistry (Levy et al., 2018).
525 Higher model resolutions can locally enhanced density gradients (Levy et al., 2012; Omand et al.,
526 2015) leading to ageostrophic circulations that perturbs the circular flow around vortices (Martin and
527 Richards, 2001) or enhanced vertical velocities that potentially foster the nutrient supply to the
528 euphotic layer. Beside the mesoscale Ekman pumping located at the eddy center, eddy-wind
529 interactions also produce vertical velocities at the eddy periphery (e.g. Flierl and McGillicuddy, 2002).
530 Finally, it is also worth noting that anticyclonic mesoscales eddies are capable of trapping near-inertial
531 energy waves in the ocean (Kunze 1985, Danioux et al. 2008, Koszalka et al. 2010, Pallas-Sanz et al.,
532 2016) where they produce vertical recirculation patterns (Zhong and Bracco, 2013). Even if, some of
533 these dynamical aspects are partially resolved at $1/12^\circ$ horizontal resolution, higher resolutions
534 simulations are necessary to correctly assess their specific impact.



535 **Acknowledgments:** Research funded by the National Council of Science and Technology of Mexico –
536 Mexican Ministry of Energy – Hydrocarbon Trust, project 201441. This is a contribution of the Gulf of
537 Mexico Research Consortium (CIGoM). We acknowledge the provision of supercomputing facilities
538 by CICESE.



539 **APPENDIX A: CHL/C-biomass ratio and ecosystem structure**

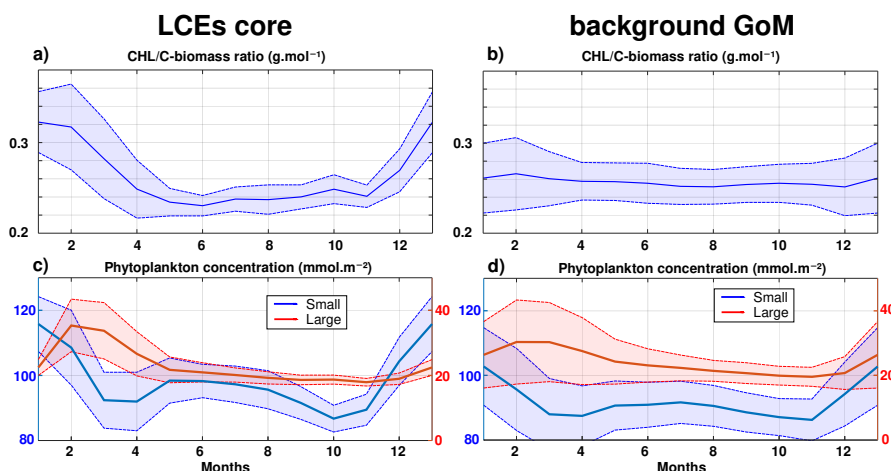
540 [CHL] is widely used as a proxy for photosynthetic biomass (Strickland, 1965; Cullen, 1982).
541 However, in addition to depend on phytoplankton concentration, it is also affected by several other
542 factors mainly produced by intracellular physiological mechanisms (Geider, 1987). In particular,
543 photoacclimation processes have been proved to be determinant to explain [CHL]_{surf} variability in
544 oligotrophic areas (Mignot et al. 2014). In the GoM open-waters, this issue was specifically addressed
545 at a basin scale in Pasqueron de Fommervault et al. (2017) considering in-situ particulate
546 backscattering measurements and in Damien et al. (2018) from modeling tools. They both reach the
547 same conclusion: [CHL]_{tot} variability provides a reasonably good estimate of the total C-biomass
548 variability ([PHY]_{tot}).

549 This is confirmed by the small amplitude of the seasonal cycle of the ratio [CHL]_{tot}/[PHY]_{tot} in
550 the background GoM (0.256 +/- 0.004 g·mol⁻¹ averaged throughout the year, Fig A1). In the LCEs
551 core, this statement is still valid but must be qualified, since the ratio [CHL]_{tot}/[PHY]_{tot} presents small
552 but significant changes through the year (Fig A1.a). It is around 0.24 g·mol⁻¹ from March to November
553 and increases sharply in December to reach about 0.32 g·mol⁻¹ in January and February. As a result, in
554 winter, the photoacclimation mechanism accounts for ~25% of the total [CHL]_{tot} increase (the
555 remaining part being an effective phytoplankton biomass increase). In summer, the ratio
556 [CHL]_{tot}/[PHY]_{tot} is slightly lower in the LCEs core compared to the background GoM. As a
557 consequence, the [CHL]_{tot} negative anomaly associated with LCEs core does not necessarily translate
558 into a [PHY]_{tot} negative anomaly.

559 Overall in the GoM open-waters, there is a dominance of the small-size phytoplankton over the
560 large-size class in proportion closed to 80%-20% (Linacre et al., 2015). Although the modeled



561 ecosystem structure is relatively simple, this typical community size structure is well reproduced by
562 GOLFO12-PISCES (Fig A1.c and A1.d), that also suggests a shift in the ecosystem structure in winter.
563 The different response among size classes results from the enhancement of nutrient vertical flux. The
564 role of “secondary” nutrient in this change in the community composition must not be overlooked also,
565 in particular for diatoms (accounted in the model’s large-size group) since they also uptake on silicate
566 (Benitez-Nelson et al., 2007). Moreover, GOLFO12-PISCES exhibits a modulation of the ecosystem
567 structure by LCEs. The dominance of small-size phytoplankton is slightly more marked in summer and
568 the winter shift is stronger in the LCEs core.



569 **Figure A1:** Climatological seasonal cycles of (a and b) the CHL/C-biomass ratio and (c and d) the vertically integrated content of
570 phytoplankton concentration (small size in blue, large size in red). The left panels (a and c) refer to the time series in the LCEs
571 core ($r < 50$ km) whereas the right panels (b and d) refer to the time series in the background GoM ($r > 200$ km). For each
572 average cycle, the average value is shown (full line) along with its variability (± 1 standard deviation relative to the mean, dashed
573 lines).



574 ***APPENDIX B : Nitrate budget at a seasonal scale***

575 Nutrients availability in the euphotic layer is a key mechanism to trigger biomass increase in
 576 LCEs. The processes driving the seasonality of nutrient concentrations are here investigated diagnosing
 577 the different contributions to nitrate concentrations (hereafter [NO₃]) variability. The goal is to confirm
 578 the vertical transport of nutrients and quantify the budget in order to determine the driving mechanisms.
 579 The analysis is restricted to nitrate concentrations, considered as the main limiting factor for large size-
 580 class phytoplankton growth in the GoM (Myers et al., 1981; Turner et al., 2006), although phosphates
 581 and silicates are also modeled. We do not exclude that phosphates or silicates could also play a
 582 significant role. In cylindrical coordinates, the [NO₃] equation reads:

$$\begin{aligned}
 \frac{\partial NO_3}{\partial t} = & \underbrace{-V_r \frac{\partial NO_3}{\partial r}}_{\text{radial advection}} - \underbrace{\frac{V_\theta}{r} \frac{\partial NO_3}{\partial \theta}}_{\text{azimuthal advection}} - \underbrace{V_z \frac{\partial NO_3}{\partial z}}_{\text{vertical advection}} + \underbrace{\frac{D_l}{r} \frac{\partial}{\partial r} \left(r \frac{\partial NO_3}{\partial r} \right) + \frac{D_l}{r^2} \frac{\partial^2 NO_3}{\partial \theta^2}}_{\text{lateral diffusion}} \\
 & + \underbrace{\frac{\partial}{\partial z} \left(K_z \frac{\partial NO_3}{\partial z} \right)}_{\text{vertical diffusion}} + \underbrace{SMS}_{\text{Source minus sink}} + \text{Asselin}
 \end{aligned}$$

583

584 Basically, this is a 3D advection-diffusion equation with added "sources and sinks" terms, namely
 585 biogeochemical release and uptake rates. One must include also an "Asselin term", a modeling artifact
 586 due to the Asselin time filtering. We focus on the seasonal cycle of three particular trend terms: the
 587 vertical mixing (Fig B1.a and B1.b), the vertical advection (Fig B1.c and B1.d) and a "source minus
 588 sink" term (Fig B1.e B1.f).

589 [NO₃] variations from vertical dynamics are mainly positive, especially in the first 100 m of the
 590 water column. This traduces in year-round NO₃ source driven by physical processes. By contrast,
 591 biogeochemical processes consume NO₃ in the upper layer to sustain the primary production (Fig B1.e
 592 and B1.f). In the sub-surface layer (~ below the isoline on which nitrate concentration is equal to 2
 593 mmol.m⁻³), the process of nitrification constitutes a biological source of [NO₃]. To first order, this



594 represents the global functioning of the ecosystem, valid in both fields and throughout the year.
595 However, the seasonal cycle strongly influence the magnitude of these trend terms, in particular in the
596 LCE core.

597 In winter, from December to February, vertical advective and diffusive motions produce an
598 increase of $[\text{NO}_3]$ within the mixed layer. This tendency consists in an advective entrainment resulting
599 from the deepening of the mixed layer which mainly acts to increase $[\text{NO}_3]$ at the base of the mixed
600 layer (Fig B1.c and B1.d) and vertical mixing which redistributes vertically the nutrients and tends to
601 homogenize $[\text{NO}_3]$ in the mixed layer (Fig B1.a and B1.b). The winter $[\text{NO}_3]$ increase is most important
602 in the LCE core at the base of the mixed layer ($\sim + 6.5 \cdot 10^{-7} \text{ mmol} \cdot \text{m}^{-3} \cdot \text{d}^{-1}$, nearly 3 times larger than in
603 the background GoM), attesting here a preferential NO_3 uplift due to deeper convection. Integrated
604 over the mixed layer, the winter vertical fluxes produce $[\text{NO}_3]$ enhancement of $\sim 2.4 \cdot 10^{-5} \text{ mmol} \cdot \text{m}^{-2} \cdot \text{d}^{-1}$
605 in the eddy core whereas it is only of $\sim 1.6 \cdot 10^{-5} \text{ mmol} \cdot \text{m}^{-2} \cdot \text{d}^{-1}$ in the background GoM. This also
606 explains why, on average, the density/nitrate relation differs in the LCEs core (Fig 5.e). In response, the
607 $[\text{NO}_3]$ tendency due to biogeochemical processes indicates an increase of the $[\text{NO}_3]$ uptake. This
608 increase is about 1.5 times larger in the core ($\sim - 1.3 \cdot 10^{-3} \text{ mmol} \cdot \text{m}^{-2} \cdot \text{d}^{-1}$ integrated over the mixed layer)
609 than in the background GoM ($\sim - 0.9 \cdot 10^{-3} \text{ mmol} \cdot \text{m}^{-2} \cdot \text{d}^{-1}$). Knowing that it feeds biomass production, this
610 $[\text{NO}_3]$ loss is consistent with the primary production peak in winter (Fig 9.e and 9.f).

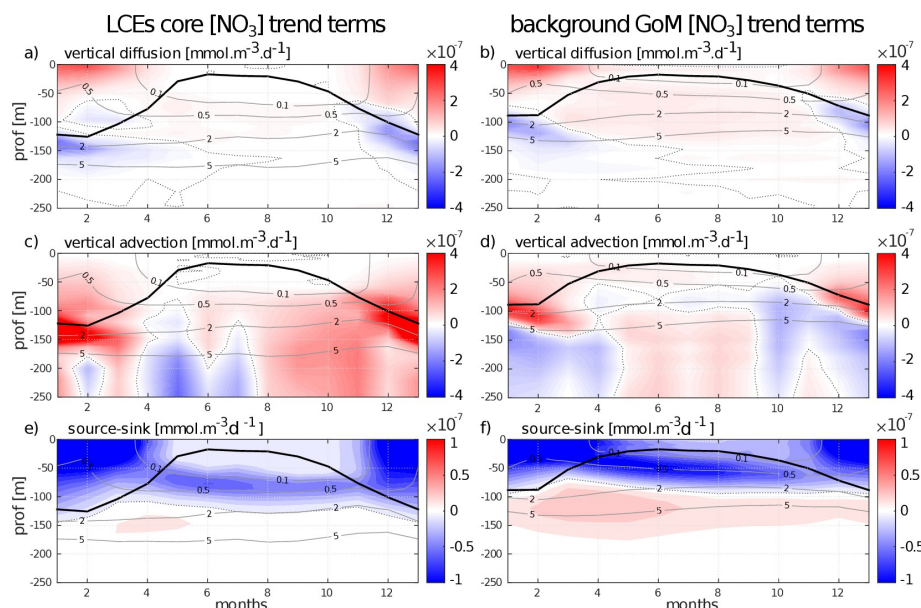
611

612 In summer, $[\text{NO}_3]$ variations due to vertical processes are smaller than in winter. They are also
613 weaker in the LCEs core upper layer (almost nil in the 0-50m layer) compared to the background GoM,
614 consistent with a deeper NO_3 pool and a shallow mixer layer. In the eddy core, one can assume that the
615 NO_3 vertical supply is entirely consumed before reaching 50m. Below 50m, vertical $[\text{NO}_3]$ diffusive
616 trends are consistently more important in the background GoM, in agreement with a steeper nitracline
617 (Fig 5.e). In contrast, vertical $[\text{NO}_3]$ advective trends in the eddy core are similar to or can eventually



618 exceed the trends in the background GoM (as in September and October for example). This confirms a
619 pumping mechanism to sustain primary production in summer within the eddy core (section V.4) The
620 biogeochemical activity related to $[\text{NO}_3]$ variations is also less intense in summer compared to winter.
621 The depth of maximum $[\text{NO}_3]$ uptake is located just above the DCM and $[\text{NO}_3]$ release below. The loss
622 of $[\text{NO}_3]$ is about twice larger in the background GoM ($\sim -0.9 \cdot 10^{-7} \text{ mmol} \cdot \text{m}^{-3} \cdot \text{d}^{-1}$) than in the LCEs core
623 ($\sim -0.5 \cdot 10^{-7} \text{ mmol} \cdot \text{m}^{-3} \cdot \text{d}^{-1}$). It is noteworthy that the biogeochemical $[\text{NO}_3]$ source term, namely the
624 nitrification rate, is really low within the eddy core.

625 To close this analysis of the $[\text{NO}_3]$ budget, it must be said that lateral diffusion and Asselin
626 tendencies are marginal terms compared to the others. Horizontal advection is of the same order of
627 magnitude as the vertical terms and mainly acts to redistribute horizontally the NO_3 vertically moved
628 (see supplementary material 1).



629 **Figure B1: Seasonal cycle of nitrate trend terms in the (left column) LCEs core and in the (right column) background GoM. The**
630 **trend induced by (a and b) vertical mixing, the (c and d) vertical advection and the (e and f) biogeochemical source minus sink are**
631 **represented. Isopycnals anomalies (gray contours) and the depth of the mixed layer (black line) are superimposed.**



632 **REFERENCES:**

- 633 Ascani, F., Richards, K. J., Firing, E., Grant, S., Johnson, K. S., Jia, Y., et al. (2013). Physical and
634 biological controls of nitrate concentrations in the upper subtropical North Pacific Ocean. *Deep Sea*
635 *Research, Part II*, 93, 119–134.
- 636 Aumont, O., & Bopp, L. (2006). Globalizing results from ocean in situ iron fertilization studies. *Global*
637 *Biogeochemical Cycles*, 20, GB2017. <https://doi.org/10.1029/2005GB002591>.
- 638 Aumont, O., Ethé, C., Tagliabue, A., Bopp, L., & Gehlen, M. (2015). PISCES-v2: An ocean
639 biogeochemical model for carbon and ecosystem studies. *Geoscientific Model Development*, 8(8),
640 2465–2513.
- 641 Badan Jr, A., Candela, J., Sheinbaum, J., & Ochoa, J. (2005). Upper-layer circulation in the approaches
642 to Yucatan Channel. *Washington DC American Geophysical Union Geophysical Monograph*
643 *Series*, 161, 57-69.
- 644 Barnett, T. P., Pierce, D. W., & Schnur, R. (2001). Detection of anthropogenic climate change in the
645 world's oceans. *Science*, 292(5515), 270-274.
- 646 Behrenfeld, M. J., O'Malley, R. T., Siegel, D. A., McClain, C. R., Sarmiento, J. L., Feldman, G. C., ...
647 & Boss, E. S. (2006). Climate-driven trends in contemporary ocean productivity. *Nature*, 444(7120),
648 752.



- 649 Benitez-Nelson, C. R., Bidigare, R. R., Dickey, T. D., Landry, M. R., Leonard, C. L., Brown, S. L., ...
650 & Bibby, T. S. (2007). Mesoscale eddies drive increased silica export in the subtropical Pacific Ocean.
651 *Science*, 316(5827), 1017-1021.
- 652 Biggs, D. C., & Ressler, P. H. (2001). Distribution and abundance of phytoplankton, zooplankton,
653 ichthyoplankton, and micronekton in the deepwater Gulf of Mexico. *Gulf of Mexico Science*, 19(1), 2.
- 654 Bracco, A., Provenzale, A., & Scheuring, I. (2000). Mesoscale vortices and the paradox of the
655 plankton. *Proceedings of the Royal Society of London B: Biological Sciences*, 267(1454), 1795-1800.
- 656 Brokaw, R. J., Subrahmanyam, B., & Morey, S. L. (2019), Loop current and eddy driven salinity
657 variability in the Gulf of Mexico, *Geophysical Research Letters*, 46, 5978–5986,
658 <https://doi.org/10.1029/2019GL082931>.
- 659 Chelton, D., DeSzoeko, R., Schlax, M., El Naggar, K., & Siwertz, N. (1998). Geographical variability
660 of the first baroclinic Rossby radius of deformation. *Journal of Physical Oceanography*, 28(3), 433–
661 460.
- 662 Ciani, D., Carton, X., Aguiar, A. B., Peliz, A., Bashmachnikov, I., Ienna, F., ... & Santoleri, R. (2017).
663 Surface signature of Mediterranean water eddies in a long-term high-resolution simulation. *Deep Sea*
664 *Research Part I: Oceanographic Research Papers*, 130, 12-29.
- 665 Cooper, C., Forristall, G. Z., & Joyce, T. M. (1990). Velocity and hydrographic structure of two Gulf of
666 Mexico warm-core rings. *Journal of Geophysical Research: Oceans*, 95(C2), 1663-1679.



- 667 Cullen, J. J. (1982). The deep chlorophyll maximum: Comparing vertical profiles of chlorophyll a.
668 Canadian Journal of Fisheries and Aquatic Sciences, 39(5), 791–803.
- 669 Damien, P., Pasqueron de Fommervault, O., Sheinbaum, J., Jouanno, J., Camacho-Ibar, V. F., &
670 Duteil, O. (2018). Partitioning of the Open Waters of the Gulf of Mexico Based on the Seasonal and
671 Interannual Variability of Chlorophyll Concentration. *Journal of Geophysical Research: Oceans*.
- 672 Danioux, E., Klein, P., & Rivière, P. (2008). Propagation of wind energy into the deep ocean through a
673 fully turbulent mesoscale eddy field. *Journal of Physical Oceanography*, 38(10), 2224-2241.
- 674 Dewar, W., and G. Flierl (1987), Some effects of the wind on rings, *J. Phys. Oceanogr.*, 17(10), 1653–
675 1667.
- 676 Doney, S. C., Glover, D. M., McCue, S. J., & Fuentes, M. (2003). Mesoscale variability of Sea-viewing
677 Wide Field-of-view Sensor (SeaWiFS) satellite ocean color: Global patterns and spatial scales. *Journal*
678 *of Geophysical Research: Oceans*, 108(C2).
- 679 Dong, C., X. Lin, Y. Liu, F. Nencioli, Y. Chao, Y. Guan, D. Chen, T. Dickey, and J. C. McWilliams
680 (2012), Three-dimensional oceanic eddy analysis in the Southern California Bight from a numerical
681 product, *J. Geophys. Res.*, 117, C00H14, doi:10.1029/2011JC007354.
- 682 Donohue, Kathleen A., et al. "Loop current eddy formation and baroclinic instability." *Dynamics of*
683 *Atmospheres and Oceans* 76 (2016): 195-216.



684 d'Ovidio, F., De Monte, S., Della Penna, A., Cotté, C., & Guinet, C. (2013). Ecological implications of
685 eddy retention in the open ocean: a Lagrangian approach. *Journal of Physics A: Mathematical and*
686 *Theoretical*, 46(25), 254023.

687 Dufois, F., Hardman-Mountford, N. J., Greenwood, J., Richardson, A. J., Feng, M., Herbette, S., &
688 Matear, R. (2014). Impact of eddies on surface chlorophyll in the South Indian Ocean. *Journal of*
689 *Geophysical Research: Oceans*, 119(11), 8061-8077.

690 Dufois, F., Hardman-Mountford, N. J., Greenwood, J., Richardson, A. J., Feng, M., & Matear, R. J.
691 (2016). Anticyclonic eddies are more productive than cyclonic eddies in subtropical gyres because of
692 winter mixing. *Science advances*, 2(5), e1600282.

693 Dufois, F., Hardman-Mountford, N. J., Fernandes, M., Wojtasiewicz, B., Shenoy, D., Slawinski, D., ...
694 & Toresen, R. (2017). Observational insights into chlorophyll distributions of subtropical South Indian
695 Ocean eddies. *Geophysical Research Letters*, 44(7), 3255-3264.

696 Dugdale, R. C., and J. J. Goering (1967), Uptake of new and regenerated forms of nitrogen in primary
697 productivity, *Limnol. Oceanogr.*, 12, 196–206

698 Early, J. J., Samelson, R. M., & Chelton, D. B. (2011). The evolution and propagation of
699 quasigeostrophic ocean eddies. *Journal of Physical Oceanography*, 41(8), 1535-1555.

700 Elliott, B. A. (1982). Anticyclonic rings in the Gulf of Mexico. *Journal of Physical Oceanography*,
701 12(11), 1292-1309.



- 702 Eppley, R. W., and B. J. Peterson (1979), Particulate organic matter flux and planktonic new
703 production in the deep ocean, *Nature*, 282, 677–680.
- 704 Falkowski, P., D. Ziemann, Z. Kolber, and P. Bienfang (1991), Role of eddy pumping in enhancing
705 primary production in the ocean, *Nature*, 352(6330), 55–58.
- 706 Flierl, G. R. (1981). Particle motions in large-amplitude wave fields. *Geophysical & Astrophysical*
707 *Fluid Dynamics*, 18(1-2), 39-74.
- 708 Flierl, G. R., & McGillicuddy, D. J. (2002). Mesoscale and submesoscale physical-biological
709 interactions. *The sea*, 12, 113-185.
- 710 de Fommervault, O. P., Perez-Brunius, P., Damien, P., Camacho-Ibar, V. F., & Sheinbaum, J. (2017).
711 Temporal variability of chlorophyll distribution in the Gulf of Mexico: bio-optical data from profiling
712 floats. *Biogeosciences*, 14(24), 5647.
- 713 Forristall, G. Z., Schaudt, K. J., & Cooper, C. K. (1992). Evolution and kinematics of a Loop Current
714 eddy in the Gulf of Mexico during 1985. *Journal of Geophysical Research: Oceans*, 97(C2), 2173-
715 2184.
- 716 Frolov, S. A., et al. "Loop Current eddy interaction with the western boundary in the Gulf of Mexico."
717 *Journal of physical oceanography* 34.10 (2004): 2223-2237.



- 718 Garcia-Jove Navarro, M., Sheinbaum Pardo, J., & Jouanno, J. (2016). Sensitivity of Loop Current
719 metrics and eddy detachments to different model configurations: The impact of topography and
720 Caribbean perturbations. *Atmosfera*, 29(3), 235–265. <https://doi.org/10.20937/ATM.2016.29.03.05>
- 721 Garçon, V. C., Oschlies, A., Doney, S. C., McGillicuddy, D., & Waniek, J. (2001). The role of
722 mesoscale variability on plankton dynamics in the North Atlantic. *Deep Sea Research Part II: Topical*
723 *Studies in Oceanography*, 48(10), 2199-2226.
- 724 Gaube, P., Chelton, D. B., Strutton, P. G., & Behrenfeld, M. J. (2013). Satellite observations of
725 chlorophyll, phytoplankton biomass, and Ekman pumping in nonlinear mesoscale eddies. *Journal of*
726 *Geophysical Research: Oceans*, 118(12), 6349-6370.
- 727 Gaube, P., McGillicuddy, D. J., Chelton, D. B., Behrenfeld, M. J., & Strutton, P. G. (2014). Regional
728 variations in the influence of mesoscale eddies on near-surface chlorophyll. *Journal of Geophysical*
729 *Research: Oceans*, 119(12), 8195-8220.
- 730 Gaube, P., Chelton, D. B., Samelson, R. M., Schlax, M. G., & O'Neill, L. W. (2015). Satellite
731 observations of mesoscale eddy-induced Ekman pumping. *Journal of Physical Oceanography*, 45(1),
732 104-132.
- 733 Geider, R. J. (1987), Light and temperature dependence of the carbon to chlorophyll a ratio in
734 microalgae and cyanobacteria: implications for physiology and growth of phytoplankton, *New Phytol.*,
735 106, 1–34.



- 736 Geider, R. J., MacIntyre, H. L., & Kana, T. M. (1997). A dynamical model of phytoplankton growth
737 and acclimation: Response of the balanced growth rate to light, nutrient limitation and temperature.
738 *Marine Ecology Progress Series*, 148, 187–200.
- 739 Glenn, S. M., and C. C. Ebbesmeyer (1993), Drifting buoy observations of a loop current
740 anticyclonic eddy, *J. Geophys. Res.*, , 98, 20, doi:10.1029/93JC02078.
- 741 Green, R. E., Bower, A. S., & Lugo-Fernández, A. (2014). First autonomous bio-optical profiling float
742 in the Gulf of Mexico reveals dynamic biogeochemistry in deep waters. *PloS one*, 9(7), e101658.
- 743 Guo, M., P. Xiu, S. Li, F. Chai, H. Xue, K. Zhou, and M. Dai (2017), Seasonal variability and
744 mechanisms regulating chlorophyll distribution in mesoscale eddies in the South China Sea, *J.*
745 *Geophys. Res. Oceans*, 122, 5329–5347, doi:10.1002/2016JC012670.
- 746 Hamilton, P., Leben, R., Bower, A., Furey, H., & Pérez-Brunius, P. (2018). Hydrography of the Gulf of
747 Mexico Using Autonomous Floats. *Journal of Physical Oceanography*, 48(4), 773-794. DOI: 10.1175/
748 JPO-D-17-0205.1
- 749 Hamilton, P. (2007). Eddy statistics from Lagrangian drifters and hydrography for the northern Gulf of
750 Mexico slope. *Journal of Geophysical Research*, 112, C09002. <https://doi.org/10.1029/2006JC003988>
- 751 He, Q., Zhan, H., Shuai, Y., Cai, S., Li, Q. P., Huang, G., & Li, J. (2017). Phytoplankton bloom
752 triggered by an anticyclonic eddy: The combined effect of eddy Ekman pumping and winter mixing.
753 *Journal of Geophysical Research: Oceans*, 122(6), 4886-4901.



- 754 Hernandez-Guerra, A., & Joyce, T. M. (2000). Water masses and circulation in the surface layers of the
755 Caribbean at 66 W. *Geophysical Research Letters*, 27(21), 3497–3500.
756 <https://doi.org/10.1029/1999GL011230>
- 757 Herrmann, M., Somot, S., Sevault, F., Estournel, C., & Deque, M. (2008). Modeling the deep
758 convection in the northwestern Mediterranean Sea using an eddy-permitting and an eddy-resolving
759 model: Case study of winter 1986–1987. *Journal of Geophysical Research*, 113, C04011.
760 <https://doi.org/10.1029/2006JC003991>
- 761 Huang, J., & Xu, F. (2018). Observational evidence of subsurface chlorophyll response to mesoscale
762 eddies in the North Pacific. *Geophysical Research Letters*, 45, 8462–8470.
763 <https://doi.org/10.1029/2018GL078408>
- 764 Jouanno, J., Ochoa de la Torre, J. L., Pallas Sanz, E., Sheinbaum Pardo, J., Andrade Canto, F., Candela
765 Perez, J., et al. (2016). Loop current frontal eddies: Formation along the Campeche Bank and impact of
766 coastally trapped waves. *Journal of Physical Oceanography*, 46(11), 3339–3363.
767 <https://doi.org/10.1175/JPO-D-16-0052.1>
- 768 Klein, P., & Lapeyre, G. (2009). The oceanic vertical pump induced by mesoscale and submesoscale
769 turbulence. *Annual review of marine science*, 1, 351-375.
- 770 Koszalka, I. M., Ceballos, L., & Bracco, A. (2010). Vertical mixing and coherent anticyclones in the
771 ocean: the role of stratification. *Nonlinear Processes in Geophysics*, 17(1), 37-47.



- 772 Kouketsu, S., Tomita, H., Oka, E., Hosoda, S., Kobayashi, T., & Sato, K. (2011). The role of meso-
773 scale eddies in mixed layer deepening and mode water formation in the western North Pacific. In *New*
774 *Developments in Mode-Water Research* (pp. 59-73). Springer, Tokyo.
- 775 Kunze, E. (1985). Near-inertial wave propagation in geostrophic shear. *Journal of Physical*
776 *Oceanography*, 15(5), 544-565.
- 777 Lascaratos, A., & Nittis, K. (1998). A high-resolution three-dimensional numerical study of
778 intermediate water formation in the Levantine Sea. *Journal of Geophysical Research*, 103(C9), 18497–
779 18511.
- 780 Lehahn, Y., F. d’Ovidio, M. Levy, Y. Amitai, and E. Heifetz (2011), Long range transport of a quasi
781 isolated chlorophyll patch by an Agulhas ring, *Geophys. Res. Lett.*, 38, L16610,
782 doi:10.1029/2011GL048588.
- 783 Le Hénaff, M., Kourafalou, V. H., Morel, Y., & Srinivasan, A. (2012). Simulating the dynamics and
784 intensification of cyclonic Loop Current Frontal Eddies in the Gulf of Mexico. *Journal of Geophysical*
785 *Research: Oceans*, 117(C2).
- 786 Levitus, S. (1982). Climatological atlas of the world ocean (NOAA Prof. Pap. 13, 173 p.). Washington,
787 DC: U.S. Government Printing Office.
- 788 Lévy, M., Ferrari, R., Franks, P. J., Martin, A. P., & Rivière, P. (2012). Bringing physics to life at the
789 submesoscale. *Geophysical Research Letters*, 39(14).



- 790 Lévy, M., Franks, P.J.S. & Smith, K.S. (2018). The role of submesoscale currents in structuring marine
791 ecosystems. *Nat. Commun.*, **9**, 4758
- 792 Linacre, L., Lara-Lara, R., Camacho-Ibar, V., Herguera, J. C., Bazán-Guzmán, C., & Ferreira-Bartrina,
793 V. (2015). Distribution pattern of picoplankton carbon biomass linked to mesoscale dynamics in the
794 southern gulf of Mexico during winter conditions. *Deep Sea Research Part I: Oceanographic Research*
795 *Papers*, *106*, 55-67.
- 796 Lipphardt, B., Poje, A. C., Kirwan, A., Kantha, L., & Zweng, M. (2008). Death of three Loop Current
797 rings. *Journal of Marine Research*, *66*(1), 25-60.
- 798 Madec, G. (2016). NEMO ocean engine, Note Du Pole De Mod# elisation (Vol. 27, 406 p.). Paris,
799 France: Institut Pierre-Simon Laplace.
- 800 Mann, K. H., & Lazier, J. R. N. (2006). Dynamics of marine ecosystems (3rd ed.). Oxford, UK:
801 Blackwell Publishing.
- 802 Mahadevan, A. (2014). Ocean science: Eddy effects on biogeochemistry. *Nature*, *506*(7487), 168.
- 803 Martin, A. P., & Richards, K. J. (2001). Mechanisms for vertical nutrient transport within a North
804 Atlantic mesoscale eddy. *Deep Sea Research Part II: Topical Studies in Oceanography*, *48*(4-5), 757-
805 773.
- 806 Mayot, N., D'Ortenzio, F., Taillandier, V., Prieur, L., de Fommervault, O. P., Claustre, H., ... & Conan,
807 P. (2017). Physical and biogeochemical controls of the phytoplankton blooms in North Western



- 808 Mediterranean Sea: A multiplatform approach over a complete annual cycle (2012–2013 DEWEX
809 experiment). *Journal of Geophysical Research: Oceans*, 122(12), 9999-10019.
- 810 McClain, C. R., Signorini, S. R., & Christian, J. R. (2004). Subtropical gyre variability observed by
811 ocean-color satellites. *Deep Sea Research Part II: Topical Studies in Oceanography*, 51(1-3), 281-301.
- 812 McGillicuddy, D. J., Jr. (2016), Mechanisms of Physical-Biological-Biogeochemical Interaction at the
813 Oceanic Mesoscale, *Annu. Rev. Mar. Sci.*, 8, 125–159, doi:10.1146/annurev-marine-010814-015606.
- 814 McGillicuddy Jr, D. J., Robinson, A. R., Siegel, D. A., Jannasch, H. W., Johnson, R., Dickey, T. D., ...
815 & Knap, A. H. (1998). Influence of mesoscale eddies on new production in the Sargasso Sea. *Nature*,
816 394(6690), 263.
- 817 McGillicuddy Jr, D. J., & Robinson, A. R. (1997). Eddy-induced nutrient supply and new production in
818 the Sargasso Sea. *Deep Sea Research Part I: Oceanographic Research Papers*, 44(8), 1427-1450.
- 819 Meunier, T., Sheinbaum, J., Pallàs-Sanz, E., Tenreiro, M., Ochoa, J., Ruiz-Angulo, A., ... & de Marez,
820 C. (2020). Heat Content Anomaly and Decay of Warm-Core Rings: the Case of the Gulf of Mexico.
821 *Geophysical Research Letters*, 47(3), e2019GL085600.
- 822 Meunier, T., Tenreiro, M., Pallàs-Sanz, E., Ochoa, J., Ruiz-Angulo, A., Portela, E., et al. (2018a).
823 Intrathermocline eddies embedded within an anticyclonic vortex ring. *Geophysical Research Letters*,
824 45. <https://doi.org/10.1029/2018GL077527>



- 825 Meunier, T., Pallás-Sanz, E., Tenreiro, M., Rodriguez, E. P., Ochoa, J., Ruiz-Angulo, A., & Cusí, S.
826 (2018b). The Vertical structure of a Loop Current Eddy. *Journal of Geophysical Research: Oceans*.
- 827 Mignot, A., Claustre, H., Uitz, J., Poteau, A., D’Ortenzio, F., and Xing, X., (2014), Understanding the
828 seasonal dynamics of phytoplankton biomass and the deep chlorophyll maximum in oligotrophic
829 environments: A Bio-Argo float investigation, *Global Biogeochem. Cy.*, 28, 856–876.
- 830 Monterey, G., & Levitus, S. (1997). Seasonal variability of mixed layer depth for the World Ocean
831 (NOAA Atlas NESDIS 14, 100 p.). Silver Spring, MD: National Oceanic and Atmospheric
832 Administration.
- 833 Muller-Karger, F. E., Walsh, J. J., Evans, R. H., & Meyers, M. B. (1991). On the seasonal
834 phytoplankton concentration and sea surface temperature cycles of the Gulf of Mexico as determined
835 by satellites. *Journal of Geophysical Research*, 96(C7), 12645–12665.
- 836 Myers, V. B., & Iverson, R. I. (1981). Phosphorus and nitrogen limited phytoplankton productivity in
837 northeastern Gulf of Mexico coastal estuaries. In *Estuaries and nutrients* (pp. 569-582). Humana Press.
- 838 Nencioli, F., C. Dong, T. Dickey, L. Washburn, and J. C. McWilliams (2010), A vector geometry-
839 based eddy detection algorithm and its application to a high-resolution numerical model product and
840 high-frequency radar surface velocities in the Southern California Bight, *J. Atmos. Oceanic Technol.*,
841 27, 564–579, doi:10.1175/2009JTECHO725.1.
- 842 Nof, D., 1981: On the b-induced movement of isolated baroclinic eddies. *J. Phys. Oceanogr.*, 11, 1662–
843 1672, [https://doi.org/10.1175/1520-0485\(1981\)011,1662:OTIMOI.2.0.CO;2](https://doi.org/10.1175/1520-0485(1981)011,1662:OTIMOI.2.0.CO;2).



844 Nowlin, W. D. Jr., & Parker, C. A. (1974). Effects of a cold-air outbreak on shelf waters of the Gulf of
845 Mexico. *Journal of Physical Oceanography*, 4(3), 467–486.

846 Omand, M. M., D’Asaro, E. A., Lee, C. M., Perry, M. J., Briggs, N., Cetinić, I., & Mahadevan, A.
847 (2015). Eddy-driven subduction exports particulate organic carbon from the spring bloom. *Science*,
848 348(6231), 222-225.

849 Omand, M. M., & Mahadevan, A. (2014). Shape of the oceanic nitracline. *Biogeosciences Discussions*,
850 11, 14729–14763.

851 Oschlies, A., & Garçon, V. (1998). Eddy-induced enhancement of primary production in a model of the
852 North Atlantic Ocean. *Nature*, 394(6690), 266.

853 Pallàs-Sanz, E., Candela, J., Sheinbaum, J., Ochoa, J., & Jouanno, J. (2016). Trapping of the near-
854 inertial wave wakes of two consecutive hurricanes in the Loop Current. *Journal of Geophysical*
855 *Research: Oceans*, 121(10), 7431-7454.

856 Passalacqua, G. A., Sheinbaum, J., & Martinez, J. A. (2016). Sea surface temperature influence on a
857 winter cold front position and propagation: Air-sea interactions of the ‘Nortes’ winds in the Gulf of
858 Mexico. *Atmospheric Science Letters*, 17(5), 302–307.

859 Polovina, J. J., Howell, E. A., & Abecassis, M. (2008). Ocean's least productive waters are expanding.
860 *Geophysical Research Letters*, 35(3).



- 861 Sathyendranath, S, Brewin, RJW, Müeller, D, Brockmann, C, Deschamps, P-Y, Doerffer, R, Fomferra,
862 N, Franz, BA, Grant, MG, Hu C, Krasemann, H, Lee, Z, Maritorea, S, Devred, E, Mélin, F, Peters, M,
863 Smyth, T, Steinmetz, F, Swinton, J, Werdell, J, Regner, P (2012) Ocean Colour Climate Change
864 Initiative: Approach and Initial Results, IGARSS 2012, 2024-2027.
865 doi:10.1109/IGARSS.2012.6350979.
- 866 Sheinbaum Pardo, J., Athie De Velasco, G. E., Candela Perez, J., Ochoa de la Torre, J. L., & Romero
867 Arteaga, A. M. (2016). Structure and variability of the Yucatan and loop currents along the slope and
868 shelf break of the Yucatan channel and Campeche bank. *Dynamics of Atmospheres and Oceans*, 76,
869 217–239. <https://doi.org/10.1016/j.dynatmoce.2016.08.001>
- 870 Siegel, D. A., Behrenfeld, M. J., Maritorea, S., McClain, C. R., Antoine, D., Bailey, S. W., ... & Eplee
871 Jr, R. E. (2013). Regional to global assessments of phytoplankton dynamics from the SeaWiFS
872 mission. *Remote Sensing of Environment*, 135, 77-91.
- 873 Siegel, D. A., McGillicuddy Jr, D. J., & Fields, E. A. (1999). Mesoscale eddies, satellite altimetry, and
874 new production in the Sargasso Sea. *Journal of Geophysical Research: Oceans*, 104(C6), 13359-
875 13379.
- 876 Sosa-Gutiérrez, R., et al. "Erosion of the Subsurface Salinity Maximum of the Loop Current Eddies
877 From Glider Observations and a Numerical Model." *Journal of Geophysical Research: Oceans* 125.7
878 (2020): e2019JC015397.
- 879 Strickland, J. D. H. (1965). Production of organic matter in the primary stages of the marine food
880 chain, *Chem. Oceanogr.*, 1, 477–610.



- 881 Sturges, W., & Leben, R. (2000). Frequency of ring separations from the Loop Current in the Gulf of
882 Mexico: A revised estimate. *Journal of Physical Oceanography*, 30, 1814–1819.
- 883 Sturges, W., & Kenyon, K. E. (2008). Mean flow in the Gulf of Mexico. *Journal of Physical*
884 *Oceanography*, 38(7), 1501-1514.
- 885 Sweeney, E. N., D. J. McGillicuddy, and K. O. Buesseler (2003), Biogeochemical impacts due to
886 mesoscale eddy activity in the Sargasso Sea as measured at the Bermuda Atlantic Time-series Study
887 (BATS), *Deep Sea Res., Part II*, 50(22–26), 3017–3039, doi:10.1016/j.dsr2.2003.07.008.
- 888 Tenreiro, M., Candela, J., Sanz, E. P., Sheinbaum, J., & Ochoa, J. (2018). Near-Surface and Deep
889 Circulation Coupling in the Western Gulf of Mexico. *Journal of Physical Oceanography*, 48(1), 145-
890 161.
- 891 Travis, S., & Qiu, B. (2020). Seasonal Reversal of the Near-Surface Chlorophyll Response to the
892 Presence of Mesoscale Eddies in the South Pacific Subtropical Countercurrent. *Journal of Geophysical*
893 *Research: Oceans*, 125(3), e2019JC015752.
- 894 Turner, J. S. (1973). *Buoyancy effects in fluids* (368 p.). New York, NY: Cambridge University Press.
- 895 Turner, R. E., Rabalais, N. N., & Justic, D. (2006). Predicting summer hypoxia in the northern Gulf of
896 Mexico: Riverine N, P, and Si loading. *Marine pollution bulletin*, 52(2), 139-148.



- 897 Vukovich, F. M., 2007: Climatology of ocean features in the Gulf of Mexico using satellite remote
898 sensing data. *J. Phys. Oceanogr.*, 37, 689–707, <https://doi.org/10.1175/JPO2989.1>.
- 899 Waite, A. M., S. Pesant, D. A. Griffin, P. A. Thompson, and C. M. Holl (2007), *Oceanography*,
900 primary production and dissolved inorganic nitrogen uptake in two Leeuwin Current eddies, *Deep Sea*
901 *Res., Part II*, 54(8–10), 981–1002, doi:10.1016/j.dsr2.2007.03.001.
- 902 Wawrik, B., Paul, J., Bronk, D., John, D., Gray, M., 2004. High rates of ammonium recycling drive
903 phytoplankton productivity in the offshore Mississippi River plume. *Aquat. Microb. Ecol.* 35, 175–184.
904 <http://dx.doi.org/10.3354/ame035175>.
- 905 Weisberg, R. H., & Liu, Y. (2017). On the Loop Current penetration into the Gulf of Mexico. *Journal*
906 *of Geophysical Research: Oceans*, 122(12), 9679-9694.
- 907 Williams, R. G. (1988). Modification of ocean eddies by air-sea interaction. *Journal of Geophysical*
908 *Research: Oceans*, 93(C12), 15523-15533.
- 909 Wu, G. (1964). Stratification and circulation in the Antillean-Caribbean basins (Vol. 1). New York,
910 NY: Columbia University Press.
- 911 Zhao, J., Bower, A., Yang, J., & Lin, X. (2018). Meridional heat transport variability induced by
912 mesoscale processes in the subpolar North Atlantic. *Nature communications*, 9(1), 1124.
- 913 Zhong, Y., & Bracco, A. (2013). Submesoscale impacts on horizontal and vertical transport in the Gulf
914 of Mexico, *Journal of Geophysical Research: Oceans*, 118(10), 5651-5668.